Behavior of Noble Metals during Fractional Crystallization of Cu–Fe–Ni–(Pt, Pd, Rh, Ir, Ru, Ag, Au, Te) Sulfide Melts

E.F. Sinyakova [a], V.I. Kosyakov [b], A.S. Borisenko [a,c], N.S. Karmanov [a]

*[a] V.S. Sobolev Institute of Geology and Mineralogy, Siberian Branch of the Russian Academy of Sciences,
pr. Akademika Koptyuga 3, Novosibirsk, 630090, Russia*

*[b] A.V. Nikolaev Institute of Inorganic Chemistry, Siberian Branch of the Russian Academy of Sciences,
pr. Akademika Lavrent'eva 3, Novosibirsk, 630090, Russia*

[c] Novosibirsk State University, ul. Pirogova 2, Novosibirsk, 630090, Russia

Abstract—The method of quasi-equilibrium directional crystallization was used for experimental modeling of the behavior of noble metals in the presence of Te during the fractional crystallization of Cu- and Ni-rich sulfide magma. The experimental melt contained (mol.%): Fe = 18.5, Ni = 19.1, Cu = 16.7, S = 44.1, and Pt = Pd = Rh = Ir = Ru = Ag = Au = Te = 0.2, i.e., is similar in composition to the massive pentlandite-bornite ores of platinum-copper-nickel deposits of the Noril'sk group. The crystallized sample consists of six primary zones differing in chemical and phase compositions. The main minerals crystallizing from the melt include the following sulfide phases: bornite solid solution (bnss), quaternary solid solution (tss), described earlier in the literature, and three phases (cfpn, cnpn, npn), which we attributed to pentlandite according to their chemical composition. The primary phases crystallized from the melt decay on cooling with the formation of secondary phases. The cfpn, cnpn, and tss phases decay completely, and the npn and bnss phases, partly. As a result, secondary zoning forms in the sample. Formation of drop-like inclusions of telluride melt was observed in the end zone of the ingot. The obtained data show that pentlandites and tss are the main high-temperature concentrators of PGE, with each of the macrophases showing specific PGE accumulation. Eight types of impurity phases have been detected. They form by different mechanisms: crystallization from sulfide melt of refractory compounds, deposition from telluride melt, and formation through complete or partial decay of primary macro- and microphases. A scheme of the zonal structure of the crystallized sample and the evolution of the phase composition during fractional crystallization has been constructed. It clearly demonstrates the intricate formation of primary and secondary major-component and impurity zonings and can be used to explain the nature of the zoned structure of massive PGE-bearing pentlandite–bornite orebodies.

Keywords: system Cu–Fe–Ni–S, PGE, Te, fractional crystallization, zoning, pentlandite

INTRODUCTION

Ores from platinum-bearing sulfide copper-nickel deposits contain not only main elements, such as Fe, Cu, Ni, and S, but also accompanying elements, such as As, Te, Bi, Sn, Sb, Pb, and trace noble elements, i.e., platinum group elements (PGE), Ag, and Au. Massive orebodies of the deposits are divided into zones with different chemical and mineral compositions, which agrees well with the hypothesis that attributes their origin to fractional crystallization of sulfide magma (Distler et al., 1988; Naldrett, 2004; Barnes et al., 2006; Holwell and McDonald, 2010; Barnes and Ripley, 2016; Duran et al., 2017). Pyrrhotite ores are formed at the beginning of fractional crystallization of magma, and copper-rich ores are deposited at the final stage. Chalcopyrite, talnakhite, mooihoekite, cubanite, and bornite are the main copper ore-forming minerals. These ores also include nickel sulfides, i.e., pentlandite, godlevskite, and millerite. Copper-rich ores are characterized by high Pt, Pd, Au, and Ag contents, and relatively high As, Te, Sb, Se, and Bi contents compared to pyrrhotite and pyrrhotite-chalcopyrite ores (Genkin et al., 1981, Czamanske et al., 1992; Distler et al., 1988; Naldrett, 2004; Likhachev, 2006; Sluzhenikin and Mokhov, 2015; Dare et al., 2014; Barnes and Ripley, 2016; Duran et al., 2017; etc.). It is found that noble metal and tellur impurities may dissolve in the main ore-forming minerals. However, impurities are mostly present in the main ore-forming sulfides in the form of inclusions of native elements, alloys, intermetallics, sulfides, arsenides, tellurides, bismuthides, bismuth tellurides, etc. The inclusions are primarily formed by minerals of system Pd–Pt–Te–Bi.

Distribution peculiarities of elements in zonal orebodies qualitatively agree with fractional crystallization regularities. Each zone has its constant set of phases, but their fractions may vary. Component concentrations within zones are either constant or change smoothly, however, they change abruptly between the zones (Kosyakov and Sinyakova,

---

2010, 2014, 2017a,b; Sinyakova and Kosyakov, 2014; Sinyakova et al., 2016). The experimental results show that macrocomponent and phase distribution in directionally crystallized samples match the liquid-solid diagram. Cooling of the sample is accompanied by solid-phase reactions causing changes in its phase composition and eventually decay of the primary zones into the secondary ones (Kosyakov and Sinyakova, 2010). It is the secondary zoning that is observed in the orebodies and the experimental samples.

Unfortunately, the phase diagram of the Cu–Fe–Ni–S system and its fragments is represented in the literature by simplified models (Craig and Kullerud, 1969; Fleet and Pan, 1994; Peregoedova et al., 1995; Ballhaus et al., 2001; Kosyakov and Sinyakova, 2011; Sinyakova and Kosyakov, 2012, 2014), which makes it impossible to predict the results of fractional crystallization and makes it difficult to interpret them.

Introduction of impurities increases the component count of the system and complicates its behavior during fractional crystallization. Apparently, the impurities concentrated in the melt are eventually going to be crystallized in the form of autonomous single- or multicomponent microphases. As soon as the formation starts, an impurity subzone arises, and the whole ingot should be divided into the multitude of these subzones (Kosyakov and Sinyakova, 2010, 2015). However, the experimental results show the absence of the respective microphase sequence in the ingot (Sinyakova and Kosyakov, 2012; Distler et al., 2016; Sinyakova et al., 2016, 2017), which implies that crystallization mechanisms are fundamentally different for macro- and microcomponents.

A significant interest in behavior of various trace element ensembles of noble metals and accompanying elements favored research into mineralogy of microphase inclusions (Genkin and Evstigneeva, 1986; Cabri, 2002; Dare et al., 2014; Sluzhenikin and Mokhov, 2015; Holwell et al., 2015; Duran et al., 2017), as well as studies dedicated to measurements of impurity distribution coefficients between crystals and melts (Fleet et al., 1993; Ballhaus et al., 2001; Helmy et al., 2010; Sinyakova and Kosyakov, 2012; Sinyakova et al., 2016), and physicochemical investigations of phase relations in systems based on typical impurities (Makovicky, 2002; Helmy et al., 2007, 2010; Vymazalova et al., 2015). Contrary to other researchers using isothermal curing and quenching techniques, we studied the stated problem using directional crystallization of melts with main component compositions similar to those of natural sulfide magmas (Distler et al., 2016; Sinyakova et al., 2016, 2017; Kosyakov and Sinyakova, 2010, 2014, 2017a,b). These experiments make it possible to study impurity behavior in the wide area, where melt composition changes regularly during zonal sample formation. To understand phase formation regularities and eliminate the synergy effect of mutual influence of metalloids co-present in the samples, it appears reasonable to examine the behavior of simpler impurity ensembles, which only include one of the metalloids, for example As (Sinyakova and Kosyakov, 2012).

Formation of pentlandite-bornite associations during fractional crystallization of Cu- and Ni-rich sulfide magma was experimentally modeled in (Kosyakov and Sinyakova, 2017a). The behavior of noble metal impurities in presence of tellur during the sample crystallization is described in the present paper.

EXPERIMENT

The initial sample (mol.%): Fe 18.5, Ni 19.1, Cu 16.7, S 44.1, Pt, Pd, Rh, Ir, Ru, Ag, Au, and Te with contents of 0.2 was prepared from high-purity Cu, Fe, Ni, Pt, Pd, Rh, Ru, Ir, Ag, Au, Te (99.99%) and analytically pure sulfur (99.9999%) additionally purified from moisture by distillation under vacuum. The mixture of elements with the specified contents was heated to 1050 °C in the quartz tube evacuated to the residual pressure of 1.5×10^{-2} Pa. The sample was cured at this temperature for 24 hours, and then cooled in the air. Directional crystallization of the sample was performed using the vertical Bridgman technique. The cylindrical quartz tube with the melt was lowered from the hot furnace area to the cold area at 2.3×10^{-8} m/s. This process provided quasi-equilibrium conditions for directional crystallization. The temperature in the lower end of the quartz tube at the beginning and at the end of crystallization was 860 and 740 °C, respectively. When crystallization was finished, the tube was cooled in the turned-off furnace.

The obtained cylindrical ingot of 8.2 mm in diameter and 70 mm long was cut into 12 puck samples, each of them weighted to determine the crystallized melt fraction (g). We used these samples to prepare polished sections and study their microstructure and chemical compositions. To identify bulk compositions of the samples, the contents of the main ore-forming minerals and impurity phases, we used scanning electron microscopy and energy dispersive spectrometry (SEM/EDS). The analysis was performed at the Analytical Center for Multielemental and Isotope research (AC MEIR) SB RAS (analyst N.S. Karmanov) using a MIRA 3 LMU high-resolution microscope (Tescan Orsay Holding) equipped with an INCA Energy 450+ X-Max 80 and INCA Wave 500 X-ray microanalysis systems (Oxford Instruments Nanoanalysis Ltd). The measurements were taken under the accelerating voltage of 20 kV, electron beam current of 1.5 nA, and live spectrum acquisition time of 30 s. K-series (S, Fe, Cu, Ni) and L-series (Pd, Pt, Rh, Ru, Ir, Au, Ag, Te) X-ray radiation was used for the analysis. The following elements were used as reference: FeS_2 (S), PbTe (Te), and pure metals Fe, Cu, Ni, Pd, Rh, Ru, Ir, Pt, Au, Ag. The lower detectable concentration limit for Ir, Pt, and Au was 0.4–0.5 wt.%, and for the remaining elements 0.1–0.2 wt.%. To reduce the effect of sample microrelief on the accuracy of the analysis, spectrum acquisition on phases sized over 5 μm was performed while scanning the areas of about 10 μm². The phases with sizes below 5 μm were analyzed by the point probe. To assess the bulk composition of

multiphase areas, the sum spectrum obtained as a result of scanning the areas up to 1.5 mm² was used. Here, live spectrum acquisition time was increased to 120 s, to achieve the lower detectable concentration limit about two times as low. The analysis accuracy of the bulk composition for multiphase areas using this technique does not exceed the accuracy limits of the electron microprobe analysis (1–2% relative) as found in (Sinyakova et al., 2016) for the example of bulk composition identification for the pyrrhotite-cubanite mixture. The bulk composition of phase mixtures was calculated in the present paper based on 3–5 probes from different areas of each section along the ingot.

According to the data on changes in bulk composition of the directionally crystallized ingot depending on the crystallized melt fraction g, the change in melt composition during directional crystallization was calculated in (Kosyakov and Sinyakova, 2017a) based on the equation:

$$c_i^L = \frac{c_{i0} - \int\limits_0^g c_i^S \, dg}{1 - g}.$$

Here, c_{i0} is the concentration of the ith component in the initial ingot, c_i^S is the average concentration of the ith component at the polished section surface with coordinate g, c_i^L is the concentration of the ith component in the melt. The obtained results were used to determine component distribution coefficients between individual solid phases and the sulfide melt: $k_i^j = c_i^j/c_i^L$ (c_i^j is the concentration of the ith component in the jth phase), and to calculate averaged component distribution coefficients between the solid ingot and the sulfide melt $\kappa_i = c_i^S/c_i^L$.

To investigate phase composition, the classical electron-microprobe analysis with the use of wavelength dispersive spectrometers (WDS) was also performed using a JXA-8100 microanalyzer (Jeol Ltd) (analysts V.N. Korolyuk and E.N. Nigmatulina at AC MEIR SB RAS) (Lavrent'ev et al., 2015a). The following reference samples were used: CuFeS₂, FeNiCo, Pd, Rh, Ru, Ir, Pt, Au, Ag, and Te. The measurements were taken under the accelerating voltage of 20 kV, probe current of 50 nA, the measurement time of 10 s on the line and 5 s at the background from the left and right. The following X-ray lines were used: SK_α, FeK_α, CuK_α, NiK_α, PtL_α, IrL_α, PdL_α, RhL_α, RuL_α, AgL_β, AuM_α, TeL_α. Detection limits for elements were <0.1 wt.%. Phase compositions were calculated based on 3–10 points from different areas of the sample. Standard deviations of element contents in phases were as follows: Fe, Cu, Ni, S—0.3; Pt, Ir, Au—0.2; Pd, Rh, Ru Ag, Te—0.1 mol.%.

It was found in (Lavrent'ev et al., 2015b) that both types of microanalysis are close in their metrological parameters. The comparison of the microanalysis results for PGE minerals obtained using wavelength and energy dispersive spectrometry (Zhmodik et al., 2016) demonstrates a satisfactory level of convergence as well.

The peculiarities of identification of Au, Pt, and Ir by SEM/EDS are to be noted. M-series peaks for Au, Pt, and Ir overlap significantly due to low EDS resolution, while the spectrometer software is unable to properly perform spectrum deconvolution (line separation) in this area of the spectrum, which is probably caused by the mismatch between the actual spectrum line shapes and the model. Thus, the analytical results are distorted, and, among other things, pseudo-concentrations of elements occur. Hence, we have to use L-series radiation for these elements in the analysis, despite the lower detectable concentration limit being about twice as high than the M-series. Erroneous sulfur detection of up to 0.8 wt.% in gold-bearing samples is another consequence of this software flaw, which we are unable to bypass since the SK_α line peak is located at the tail of the AuM_β peak. A possible contamination with polishing products of gold-bearing phases due to their low hardness was also taken into account in the interpretation of the analytical results. This contamination may primarily manifest itself in inflated contents of macrocomponents, i.e., S, Fe, Ni, and Cu.

RESULTS

Usually, the presence of trace elements in the system has no effect on the macrocomponent behavior (Ryabchikov, 1965). The results of measuring the dependence of average macrocomponent and impurity concentrations in the ingot section on the crystallized melt fraction g are shown in Table 1 along with average component distribution coefficients between the solid ingot and the melt κ_i. The results in Table 1 indicate that the studied part of the ingot consists of six primary zones (Fig. 1). The chemical composition of the ingot and average macrocomponent distribution coefficients change abruptly between the adjacent zones. It should be noted that κ_{Fe} values in zones V and VI are the same within the measurement error. However, it can be seen from Table 1 that contents of Fe and other macrocomponents change abruptly between zones V and VI.

Impurity behavior in the given sample is studied in the present paper. The data on changes in Pd, Rh, and Ag contents and their average distribution coefficients along the ingot are presented in Table 1. We used detection limit values for the upper estimates of the average impurity content and its distribution coefficient in areas, where impurity contents were below the detection limit, when necessary.

We expect to discuss the behavior of trace elements, whose contents in the samples were close to the detection limit, in more detail in the future.

Impurity behavior during crystallization in different zones of the ingot is analyzed below.

Zone I ($0 \leq g \leq 0.004$). Formation of the main sulfide minerals and impurity behavior in zone I are illustrated schematically in Fig. 2. Fe- and Cu-rich pentlandite phase with bulk composition $Fe_{25.3}Ni_{18.2}Cu_{7.9}Rh_{0.6}Ir_{0.4}Ru_{0.4}S_{47.2}$ referred to below as cfpn (Table 1) is formed from the melt.
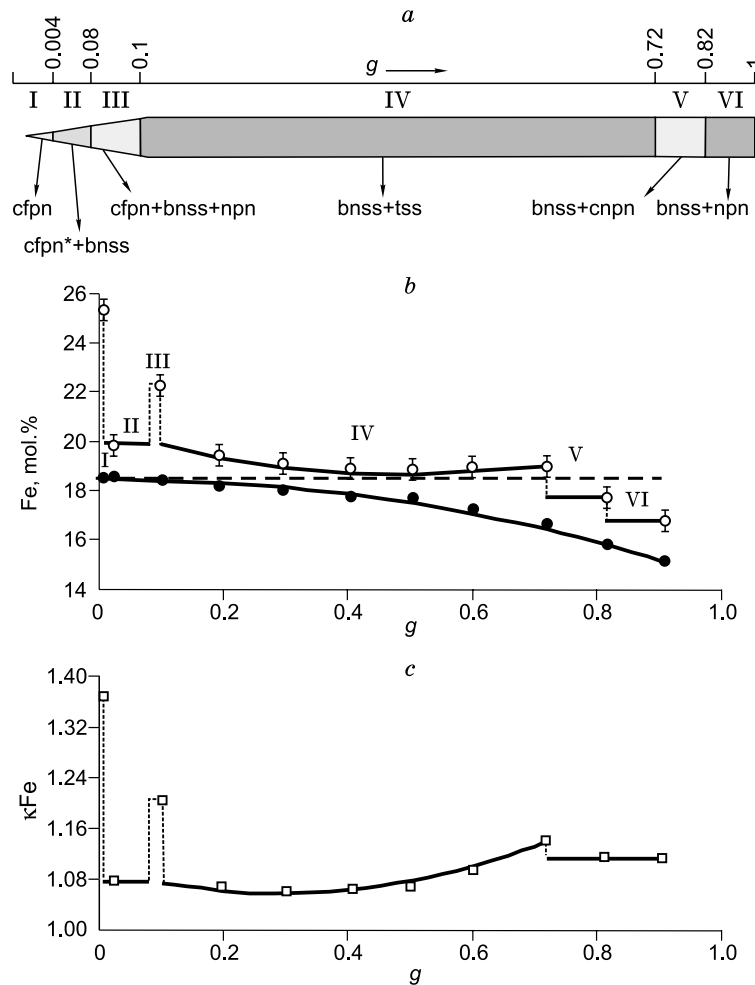
Fig. 1. Zonal structure of the directionally crystallized ingot. *a*, Schematic illustration of the primary chemical and mineral zoning based on (Kosyakov and Sinyakova, 2017a) and the present paper. The splitting of an ingot into six zones is shown; *b*, changes in average Fe contents in the ingot (light circles) and the melt (dark circles) during crystallization. The dashed line shows Fe content in the initial melt; *c*, dependence of average Fe distribution coefficients between the solid ingot and the melt (light squares) on *g*.

Fe and S are mostly transferred to the solid solution, while Cu and Ni are pushed to the melt. This phase is enriched in Ru, Rh, and Ir ($k > 1$). Palladium, Pt, Au, Ag, and Te accumulate almost exclusively in the melt, due to their contents in the ingot being below the detection limit of the electron microprobe analysis. Ruthenium impurity is isolated from the melt in the form of a refractory compound, i.e., laurite RuS_2 (with melting temperature >1600 °C (Massalsky et al., 1990)). It is present in the form of faceted crystals sized 1×0.4–$0.5\ \mu m^2$ (Fig. 3*a*, *b*, Table 2).

Temperature decrease leads to decay of the primary cfpn with formation of a finely dispersed multiphase mixture. Chemical analysis of the decay products made it possible to identify Ni-rich pentlandite (Ni/Fe = 1.1–1.2) referred to below as npn″. We present the compositions of the following two npn″ grains as examples: $Fe_{23.4}Ni_{27.5}Cu_{1.2}Pd_{0.2}Rh_{0.6}S_{47.1}$ and $Fe_{22.9}Ni_{25.5}Cu_{3.1}Ag_{0.1}Ir_{0.4}Ru_{0.4}Rh_{0.6}S_{47.0}$. In addition, iron-rich monosulfide solid solution Fe-mss $Fe_{32.7}Ni_{13.5}Cu_{1.7}Ru_{0.2}Ir_{0.4}Rh_{0.9}S_{50.6}$ and bornite solid solution bnss $Fe_{11.6}Ni_{0.1}$

$Cu_{47.9}S_{40.4}$ with composition close to stoichiometric. Micronscale inclusions of unidentified phases are present in these macrophases as well. The presented results show that Ir, Ru, and Rh are redistributed between Fe-mss and npn″, while Pd and Ag are concentrated in npn″.

Zone II (0.004 ≤ g ≤ 0.08). Primary, secondary, and impurity fractionation peculiarities during the sulfide melt crystallization in zone II are illustrated schematically in Fig. 4. Averaged ingot composition in zone II $Fe_{19.9}Ni_{12.8}Cu_{22.7}Ag_{0.2}Pd_{0.1}S_{44.3}$ is significantly enriched in copper and depleted in sulfur compared to zone I (Table 1). Binary eutectics of large lamellar inclusions with the bnss $Fe_{12.9}Ag_{0.1}Cu_{46.6}S_{40.4}$ in the matrix, whose bulk composition $Fe_{25.0}Ni_{16.9}Cu_{11.3}Pd_{0.1}S_{46.7}$ matches cfpn (Ni/Fe = 0.7) enriched in copper compared to cfpn in zone I (referred to below as cfpn*), is crystallized from the melt. Pd is dissolved in cfpn*, and Ag in bnss. The remaining impurity contents were below the detection limit.

Table 1. Average composition of the ingot and melt components and averaged component distribution coefficients between the solid ingot and the melt

g	Solid phase composition, mol.%							κ (solid/L)						
	Fe	Ni	Cu	Ag	Pd	Rh	S	Fe	Ni	Cu	Ag	Pd	Rh	S
Zone I (0 ≤ g ≤ 0.004)														
0.004	25.33	18.22	7.89	<0.1	<0.1	0.60	47.20	1.37	0.95	0.47	<0.3	<0.5	3.00	1.07
Zone II (0.004 ≤ g ≤ 0.08)														
0.03	19.88	12.85	22.74	0.16	0.11	<0.1	44.25	1.07	0.66	1.37	0.79	0.54	0.05	1.00
Zone III (0.08 ≤ g ≤ 0.10)														
0.10	22.73	18.82	11.63	0.12	<0.1	0.46	46.24	1.23	0.98	0.70	0.58	<0.5	2.42	1.05
Zone IV (0.10 ≤ g ≤ 0.72)														
0.19	19.52	18.62	16.46	0.11	0.13	0.21	44.95	1.07	0.96	0.97	0.48	0.57	1.13	1.02
0.30	19.10	19.50	16.29	0.13	0.18	0.19	44.55	1.07	1.00	0.95	0.56	0.77	1.03	1.02
0.41	18.89	19.38	16.63	0.11	0.17	0.18	44.47	1.06	0.99	0.97	0.43	0.67	0.97	1.02
0.50	18.74	19.08	17.32	0.10	0.15	0.19	44.36	1.07	0.97	1.01	<0.3	0.56	1.03	1.02
0.60	18.86	18.81	17.55	0.10	0.15	0.19	44.25	1.10	0.95	1.03	0.28	0.49	1.00	1.02
0.72	18.89	17.78	18.65	0.11	0.16	0.15	44.26	1.14	0.86	1.14	0.24	0.44	0.76	1.02
Zone V (0.72 ≤ g ≤ 0.82)														
0.82	17.67	15.33	23.00	0.23	0.19	0.11	43.47	1.11	0.65	1.81	0.42	0.43	0.45	1.01
Zone VI (0.82 ≤ g ≤ 1.0)														
0.91	16.71	23.27	14.76	0.24	0.44	0.23	44.35	1.11	0.99	1.39	0.27	0.95	0.87	1.05

Note. Ir and Ru contents in zone I are 0.4 mol.%, $\kappa_{Ir,Ru}$ = 1.8. Ir and Ru contents in the other zones, as well as Pt, Au, and Te contents below the detection limit in all ingot zones are determined by electron-microprobe analysis.

Under cooling, cfpn* phase decays into a complex mixture of daughter phases (Fig. 5a). First, these are pink grains of the nickel-rich (Ni/Fe = 1.4) pentlandite $Fe_{21.4}Ni_{30.0}Cu_{0.7}$
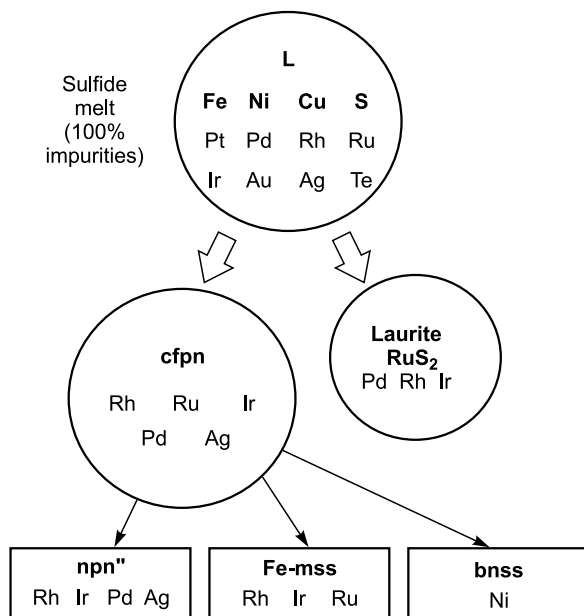

Fig. 2. Crystallization scheme of ore-forming minerals with their further decay in zone I and noble metal and tellur impurity behavior in these processes.

$Pd_{0.6}Ag_{0.1}S_{47.2}$, referred to below as npn′. Second, these are visually identical but different in compositions light brown grains, which may be attributed to haycockite hc $Fe_{27.8}Cu_{23.0}Ni_{0.8}S_{48.4}$, mooihoekite mh $Fe_{26.4}Cu_{26.2}Ni_{0.8}S_{46.6}$, and talnakhite tal $Fe_{25.4}Cu_{27.4}Ni_{0.7}S_{46.5}$. Third, these are fragments with nonuniform grayish tint and bulk composition $Fe_{21.1}Ni_{20.4}Cu_{13.1}Pd_{0.2}S_{45}$ with Ni/Fe ~ 1 and $\sum Me/S$ = 11/9. This phase was referred to as $Me_{11}S_9$ in (Kosyakov and Sinyakova, 2017a). When temperature decreases, it decays into alternating thin npn′ (Ni/Fe = 1.2) $Fe_{23.7}Ni_{27.9}Cu_{1.2}Pd_{0.4}S_{46.8}$ and bnss $Fe_{11.5}Ni_{0.3}Cu_{48.9}S_{39.3}$ plates (Fig. 5d). Fourth, small blue grains of bnss $Fe_{13.4}Ni_{0.3}Cu_{45.2}S_{41.1}$ are present in cfpn* decay products. Thus, when the primary cfpn* decays, Pd impurity is concentrated in npn′ grains. Pd impurity is also present in the phase $Me_{11}S_9$ and is transferred into npn′ upon its decay.

Noble metal microphases are crystallized from the melt simultaneously with crystallization of the main minerals both in the form of autonomous formations and their splices. Platinum forms faceted crystals of the tetragonal tetraferroplatinum phase $Pt_{1\pm x}Fe$ sized up to 6 × 6 μm² (Fig. 5b), two-phase splices with Au* sized up to 10 × 10 μm² (b, c), and three-phase splices $Pt_{1\pm x}Fe|Au*|Ag$ (5b). $Pt_{1\pm x}Fe$ includes Pd, Ir, Au, and Ag impurities (Table 2). The Au-based alloy including ~ 20 mol.% of Cu, Ag, and Pd impurities referred to below as Au* is present in the form of grains with sizes from few to 20 μm (Fig. 5b–e), the dendrite-like structure

Table 2. Representative chemical probes of noble metal microminerals formed in the crystallized sample

Mineral	Ideal formula	Fe	Ni	Cu	Au	Ag	Pt	Pd	Ru	Ir	Rh	Te	S	Total
Zone I														
Laurite	RuS_2	–	–	–	–	–	–	–	45.17	19.32	–	–	34.95	99.44
Laurite	RuS_2	–	–	–	–	–	–	–	27.29	6.14	–	–	66.57	100
Laurite	RuS_2	0.14		0.04	0.08	–	–	1.80	42.23	18.76	1.16	–	36.18	100.47
Laurite	RuS_2	0.15		0.03	0.02	–	–	1.01	24.91	5.82	0.67	–	67.29	100
Zone II														
Tetraferroplatinum	PtFe	10.38	2.97	3.07	10.9	0.56	68.13	1.79	–	–	–	–	–	97.81
Tetraferroplatinum	PtFe	26.13	7.11	6.79	7.78	0.73	49.09	2.36	–	–	–	–	–	100
Tetraferroplatinum	PtFe	11.63	3.75	3.08	3.22	–	74.47	1.35	–	1.57	–	–	–	99.07
Tetraferroplatinum	PtFe	28.16	8.64	6.55	2.21	–	51.62	1.72	–	1.1	–	–	–	100
Gold-based alloy	Au*	0.86	0.72	6.53	75.16	6.76	–	6.87	–	–	–	–	0.87	97.77
Gold-based alloy	Au*	2.31	1.84	15.42	57.26	9.40	–	9.69	–	–	–	–	4.07	100
Silver	Ag	0.69	–	2.48	–	97.40	–	–	–	–	–	0.39	–	100.96
Silver	Ag	1.29	–	4.08	–	94.31	–	–	–	–	–	0.32	–	100
Zone III														
Tetraferroplatinum	PtFe	12.43	3.51	2.88	–	–	77.06	1.39	–	2.47	–	–	–	99.73
Tetraferroplatinum	PtFe	29.73	7.99	6.05	–	–	52.76	1.75	–	1.72	–	–	–	100
Gold-based alloy	Au*	1.72	0.48	8.4	74.11	9.28	–	7.95	–	–	–	–	1.23	103.18
Gold-based alloy	Au*	4.13	1.1	17.71	50.4	11.52	–	10.01	–	–	–	–	5.14	100
Silver	Ag	0.24	–	0.75	–	98.56	–	–	–	–	–	0.43	–	99.98
Silver	Ag	0.47	–	1.26	–	97.90	–	–	–	–	–	0.37	–	100
Zone IV														
Isoferroplatinum	Pt_3Fe	10.12	1.46	1.29	1.58	–	85.25	–	–	–	–	–	–	99.70
Isoferroplatinum	Pt_3Fe	26.99	3.7	3.02	1.19	–	65.09	–	–	–	–	–	–	100
Isoferroplatinum	Pt_3Fe	9.97	1.39	0.98	–	–	84.86	0.36	–	2.31	–	–	–	99.88
Isoferroplatinum	Pt_3Fe	26.72	3.54	2.31	–	–	65.12	0.51	–	1.8	–	–	–	100
Isoferroplatinum	Pt_3Fe	10.13	1.36	0.88	–	–	84.5	–	–	2.07	–	–	–	98.94
Isoferroplatinum	Pt_3Fe	27.39	3.5	2.09	–	–	65.4	–	–	1.63	–	–	–	100
Tetraferroplatinum	PtFe	11.3	2.47	3.88	2.12	0.28	78.08	0.77	0.35	2.3	–	–	–	101.56
Tetraferroplatinum	PtFe	27.28	5.67	8.23	1.45	0.35	53.96	0.98	0.47	1.61	–	–	–	100
Gold-based alloy	Au*	1.57	0.35	8.44	78.54	6.85	–	4.5	–	–	–	–	0.88	101.13
Gold-based alloy	Au*	4.02	0.85	19.00	57.05	9.09	–	6.05	–	–	–	–	3.93	100
Silver	Ag	–	–	–	–	100.94	–	–	–	–	–	0.44	–	101.38
Silver	Ag	–	–	–	–	99.64	–	–	–	–	–	0.36	–	100
Zone V														
Pt–Fe alloy	$Pt_{3+x}Fe_2$	10.9	2.34	2.08	–	–	83.39	–	–	1.61	–	–	–	100.32
Pt–Fe alloy	$Pt_{3+x}Fe_2$	27.74	5.67	4.65	–	–	60.75	–	–	1.19	–	–	–	100
Pt–Fe alloy	$Pt_{3+x}Fe_2$	10.39	1.99	1.54	–	–	82.93	0.77	–	1.75	–	0.27	–	99.64
Pt–Fe alloy	$Pt_{3+x}Fe_2$	27.05	4.93	3.52	–	–	61.81	1.05	–	1.32	–	0.31	–	100
Pt–Fe alloy	$Pt_{3+x}Fe_2$	10.28	1.85	1.54	1.56	–	83.27	0.43	–	1.31	–	–	–	100.25
Pt–Fe alloy	$Pt_{3+x}Fe_2$	26.86	4.6	3.54	1.16	–	62.27	0.59	–	0.99				100
Pt–Fe alloy	$Pt_{3-x}Fe_2$	10.91	2.61	2.06	–	–	76.49	1.25	–	1.21	–	–	–	94.50
Pt–Fe alloy	$Pt_{3-x}Fe_2$	28.63	6.52	4.75	–	–	57.46	1.72	–	0.92	–	–	–	100
Tetraferroplatinum	PtFe	11.42	3.2	2.84	2.46	–	75.42	1.88	–	2.21	–	–	–	99.42
Tetraferroplatinum	PtFe	27.94	7.45	6.11	1.71	–	52.82	2.41	–	1.57	–	–	–	100
Pt–Fe–Au solid solution	Pt–Fe–Au	8.14	2.42	2.8	23.63	1.99	54.55	3.05	–	2.2	–	–	0.51	99.30
Pt–Fe–Au solid solution	Pt–Fe–Au	20.67	5.85	6.25	17.01	2.62	39.66	–	–	1.62	–	–	2.26	100
Gold-based alloy	Au*	1.79	2.05	5.99	73.59	8.18	–	7.35	–	–	–	–	0.75	99.69
Gold-based alloy	Au*	4.56	4.97	13.41	53.13	10.78	–	9.82	–	–	–	–	3.33	100

Table 2 (*continued*)

Mineral	Ideal formula	Fe	Ni	Cu	Au	Ag	Pt	Pd	Ru	Ir	Rh	Te	S	Total
Gold-based alloy	Au*	0.53	0.6	4.27	74.44	13.66	3.8	3.09	–	–	–	–	0.95	101.33
Gold-based alloy	Au*	1.42	1.53	10.03	56.44	18.91	2.91	4.34	–	–	–	–	4.43	100
Silver	Ag	0.35	0.38	0.73	0	99.35	–	–	–	–	–	–	–	100.81
Silver	Ag	0.66	0.68	1.22	0	97.44	–	–	–	–	–	–	–	100
Zone VI														
Pt–Fe alloy	Pt_3Fe_2	10.07	1.73	3.15	–	0.38	80.03	0.49	–	1.43	–	–	–	97.28
Pt–Fe alloy	Pt_3Fe_2	26.32	4.3	7.24	–	0.51	59.87	0.67	–	1.09	–	–	–	100
Pt–Fe alloy	Pt_3Fe_2	10.2	1.92	2.73	–	–	82.31	0.52	0.31	1.67	–	–	–	99.66
Pt–Fe alloy	Pt_3Fe_2	26.21	4.69	6.16	–	–	60.54	0.7	0.44	1.25	–	–		100
Gold-based alloy	Au*	0.82	0.87	4.87	76	12.39	2.31	3.2	–	–	–	–	0.91	101.38
Gold-based alloy	Au*	2.17	2.19	11.32	56.98	16.96	1.75	4.44	–	–	–	–	4.19	100
Gold-based alloy	Au*	0.87	1.3	4.53	72.4	15.03	–	4.52	–	–	–	0.29	0.61	99.55
Gold-based alloy	Au*	2.29	3.26	10.49	54.08	20.5	–	6.25	–	–	–	0.33	2.8	100
Silver	Ag	0.62	–	2.05	–	99.34	–	–	–	–	–	0.58	–	102.59
Silver	Ag	1.14	–	3.33	–	95.07	–	–	–	–	–	0.46	–	100
Results of drop-like inclusion analysis in zone VI														
Bulk composition	–	1.23	1.14	1.8	6.77	7.5	3.93	56.66	–	–	–	26.42	0.19	105.65
Bulk composition	–	2.34	2.07	3.02	3.66	7.4	2.14	56.69	–	–	–	22.04	0.63	100
Keithconnite matrix	$Pd_{3-x}Te$	1.00	1.40	1.44	–	0.70	–	68.70	–	–	–	30.23	0.12	103.59
Keithconnite matrix	$Pd_{3-x}Te$	1.87	2.49	2.37	–	0.68	–	67.45	–	–	–	24.75	0.39	100
Pt-based alloy inclusion	–	6.27	2.87	7.22	16.76	3.90	50.15	11.61	–	–	–	2.13	0.29	101.18
Pt-based alloy inclusion	–	14.25	6.21	14.42	10.8	4.59	32.62	13.85	–	–	–	2.12	1.15	100
Au-based alloy inclusion	–	1.01	1.51	3.27	61.36	20.17	–	13.14	–	–	–	1.81	0.46	102.73
Au-based alloy inclusion	–	2.42	3.45	6.9	41.77	25.07	–	16.56	–	–	–	1.9	1.92	100

Note. Composition for each phase measured in mol.% is presented in the first row, in mol.% in the second row. Dash indicates the impurity content below the detection limit in the microphase.

(*c, d*), in two-phase splices Au*|Ag and Au*|$Pt_{1\pm x}$Fe (*b, c, e*), and three-phase splices $Pt_{1\pm x}$Fe|Au*|Ag (Fig. 5*b*). Silver is isolated in the form of veinlets in bnss, at the npn'|bnss interface, in the form of elongated inclusions in cracks passing through mh, npn′, and bnss grains (Fig. 5*d, e, f*), in splices with Au* (*e*) and $Pt_{1\pm x}$Fe|Au* (*b*). Silver includes Cu, Fe, and Te impurities (Table 2).

Zone III ($0.08 \leq g \leq 0.10$). The scheme of collective behavior of macroelements and impurities in zone III as a result of the melt crystallization and subsequent solid-phase
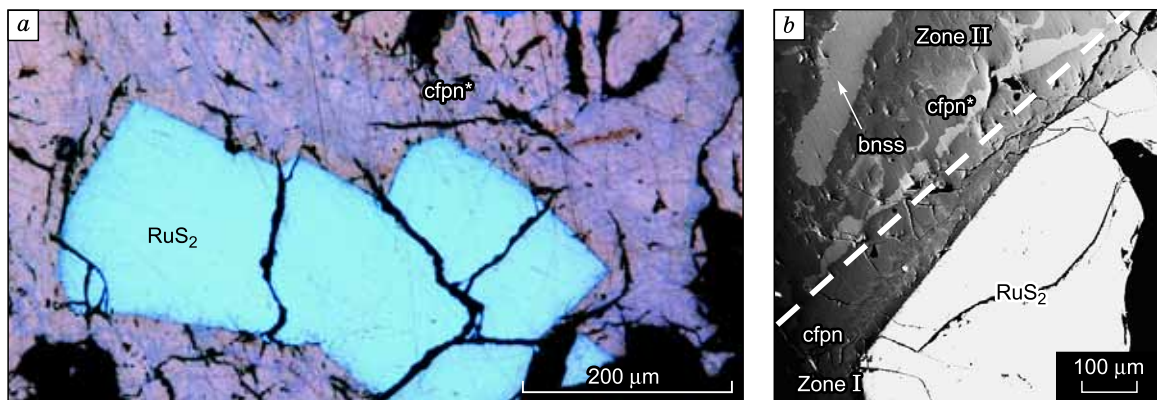

Fig. 3. Microimages of the sample in zone I in reflected light (*a*) and backscattered electrons (*b*). Faceted RuS_2 crystals are present in the finely-dispersed cfpn decay structure; dashed line indicates the interface between zones I and II.
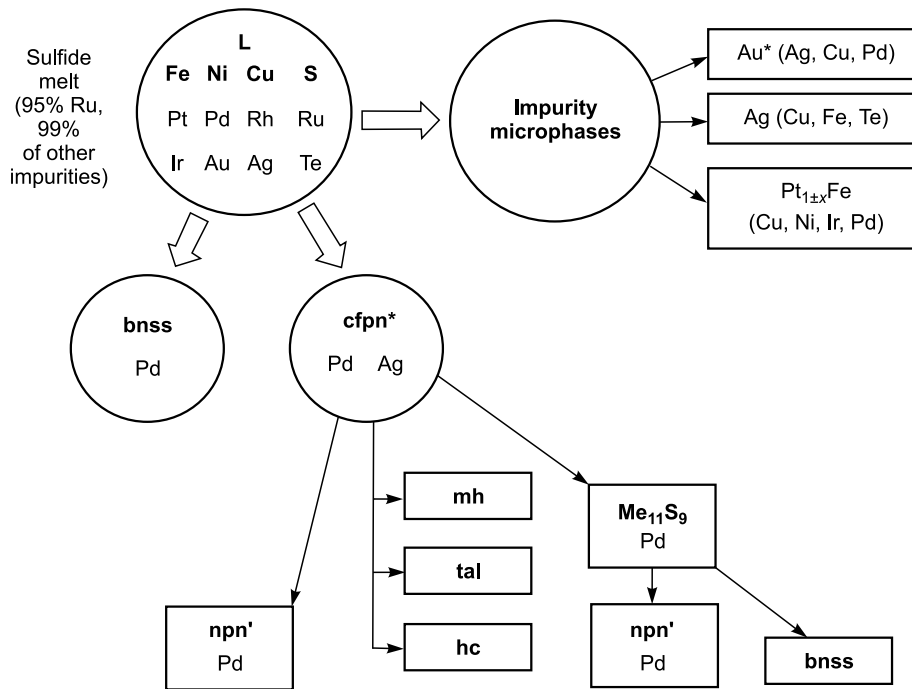
Fig. 4. Crystallization scheme of ore-forming minerals with their further decay in zone II and noble metal and tellur impurity behavior in these processes.

processes is presented in Fig. 6. The bulk composition of the ingot in zone III is $Fe_{22.7}Ni_{18.8}Cu_{11.7}Ag_{0.1}Rh_{0.5}S_{46.2}$. The ingot is enriched in iron and sulfur during the crystallization, and the melt in copper (Table 1). Triple eutectics of the nickel-rich pentlandite npn $Fe_{22.5}Ni_{27.4}Cu_{1.6}Pd_{0.1}Ru_{0.4}Ir_{0.4}Rh_{0.6}S_{47.0}$ (Ni/Fe = 1.2), bornite solid solution bnss $Fe_{13.1}Ni_{0.5}Cu_{45.3}Ag_{0.1}S_{41.0}$, and cfpn in the form of isometric gray inclusions with sizes of about 100–200 μm and the composition described by the formula $Fe_{23.6}Ni_{19.8}Cu_{7.4}Ag_{0.1}Ru_{0.6}Ir_{0.5}Rh_{0.6}S_{47.4}$ (Ni/Fe = 0.8) (Fig. 7a) is crystallized from the melt. Impurity distribution coefficients between npn and cfpn are as follows: $k_{Ru} = 0.7$, $k_{Ir} = 0.6$, $k_{Rh} = 1$.

Upon further cooling, bnss partially decays with formation of cp inclusions with composition $Fe_{25.5}Ni_{0.5}Cu_{24.6}S_{49.4}$ and Ag microinclusions. Ferriferous-cupriferous pentlandite cfpn decays upon cooling into unidentified microphases (Fig. 7a). Chemical analysis showed the presence of Ru, Ir, Rh, and Ag impurity in the mixture of this phase. The npn phase partially decays into npn″ and small Fe-mss inclusions with composition $Fe_{36.0}Ni_{10.1}Cu_{1.3}Ru_{0.4}Ir_{0.4}Rh_{0.6}S_{51.2}$. In addition to the main minerals, various noble metal impurity microphases are crystallized, such as Ag, Au*, and Pt-Fe. Platinum forms tetraferroplatinum $Pt_{1+x}Fe$, which includes Ni, Cu, Pd, and Ir impurities (Table 2). It is present in sulfide minerals in the form of faceted little crystals with sizes about 3–4 μm², but more often it forms splices $Pt_{1+x}Fe|Au$ and $Pt_{1+x}Fe|Au^*|Ag$, which enclose rounded npn″ grains (Fig. 7b, c) or is located inside chalcopyrite grains (d). Elongated Au* inclusions with lengths up to 5 μm in the form of splices with Ag and $Pt_{1+x}Fe$ are localized at cp|npn″

interphase boundaries (Fig. 7b, c). Au* inclusions and splices with Ag, as well as colonies of these inclusions are present in the secondary chalcopyrite at npn″|cp interfaces (Fig. 7c, d). Cu, Ag, and Pd impurities are dissolved in Au* (Table 2). Single-phase Ag inclusions with Cu, Fe, and Te impurities are present in the matrix bnss and sulfide matrix cracks (Fig. 7b, c, Table 2). Two-phase Ag|Au* and three-phase $Pt_{1+x}Fe|Au^*|Ag$ associations are located at npn″|bnss interfaces (Fig. 7b, c, d).

Zone IV ($0.10 \leq g \leq 0.72$). The scheme of collective behavior of macroelements and impurities in zone IV is shown in Fig. 8. This zone occupies a major part of the ingot, and therefore composition and structure of the ingot change significantly from one end of this zone to another. The bulk composition of the ingot changes from $Fe_{19.5}Ni_{18.6}Cu_{16.5}Ag_{0.1}Pd_{0.1}Rh_{0.2}S_{45.0}$ to $Fe_{18.9}Ni_{17.8}Cu_{18.6}Ag_{0.1}Pd_{0.2}Rh_{0.2}S_{44.2}$. Averaged distribution coefficients between the ingot and the melt for Fe and S are > 1, and for Cu and Ni ~ 1. Cotectics of bnss with its composition only slightly changing along the zone (from $Fe_{12.3}Ni_{0.1}Cu_{47.2}Ag_{0.1}S_{40.3}$ under $g \sim 0.2$ to $Fe_{11.2}Ni_{0.1}Cu_{48.3}Ag_{0.1}S_{40.3}$ under $g \sim 0.6$) and quaternary solid solution tss (bulk composition changes from $Fe_{20.8}Ni_{23.2}Cu_{10.3}Pd_{0.2}Rh_{0.1}S_{45.4}$ under $g \sim 0.2$ to $Fe_{19.3}Ni_{21.4}Cu_{12.6}Rh_{0.4}Ru_{0.3}Ir_{0.3}Pd_{0.1}Ag_{0.1}S_{45.5}$ under $g \sim 0.5$) is crystallized from the melt. This high-temperature unquenchable quaternary solid solution based on heazlewoodite and intermediate solid solutions, which act as its end-members in triple systems Fe–Ni–S and Cu–Fe–S, was discovered for the first time in the system Cu–Fe–Ni–S in (Peregoedova et al., 1995). At the beginning of the zone, bnss forms isometric inclusions, and
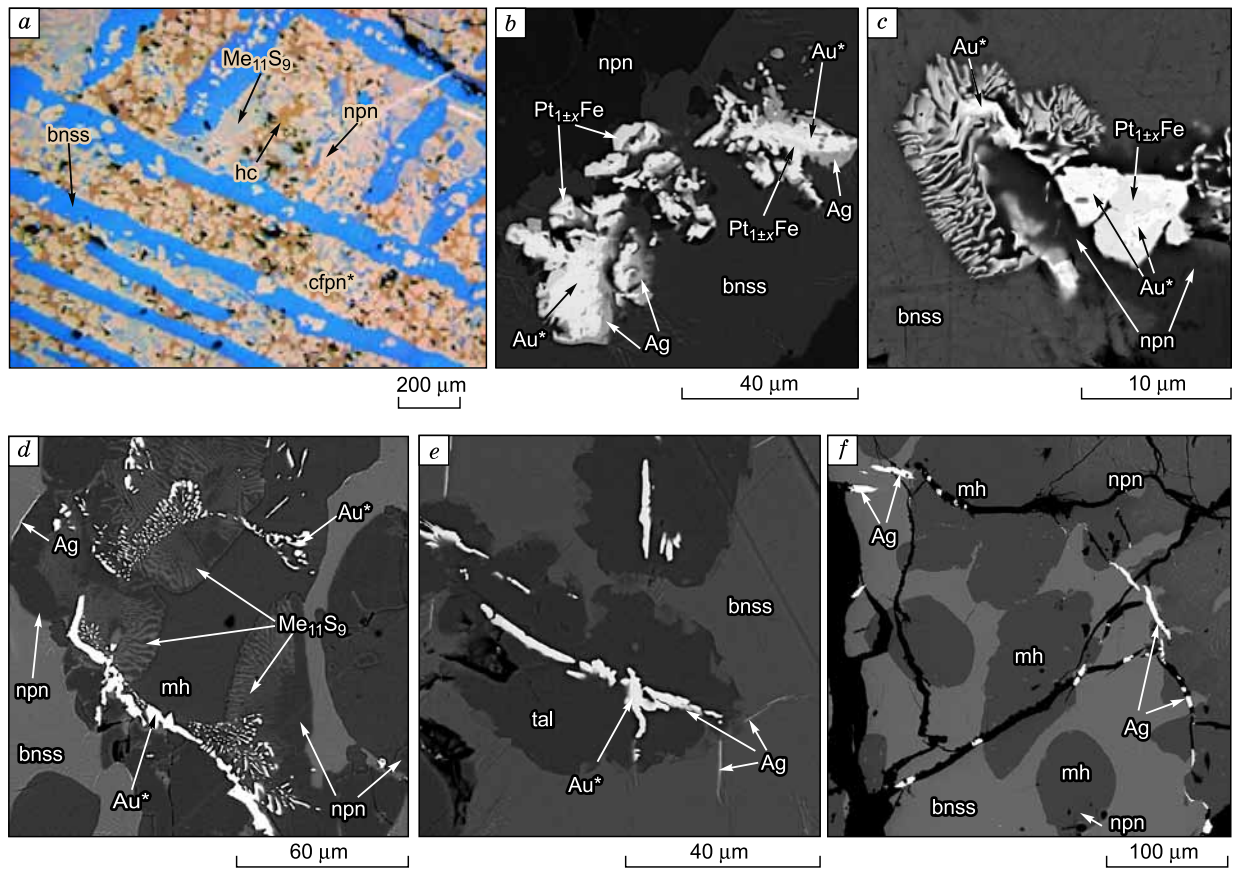
Fig. 5. Microstructures of the main ore-forming minerals and noble metal microminerals in zone II obtained in reflected light (*a*) and backscattered electrons (*b–f*). See the notes in the text.
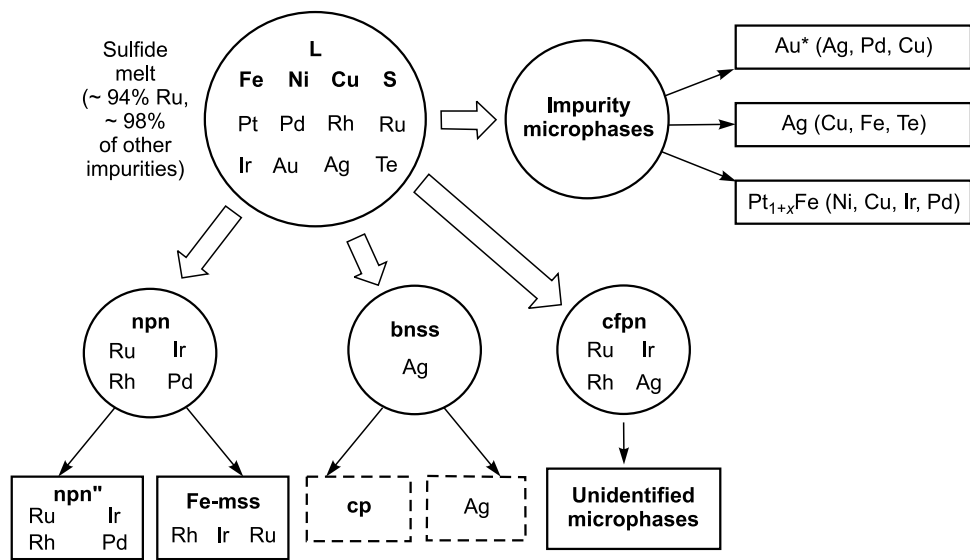

Fig. 6. Crystallization scheme of ore-forming minerals with their further decay in zone III and noble metal and tellur impurity behavior in these processes. Symbols of complete phase decay products are enclosed in solid rectangles, and symbols of partial decay products in dashed rectangles.
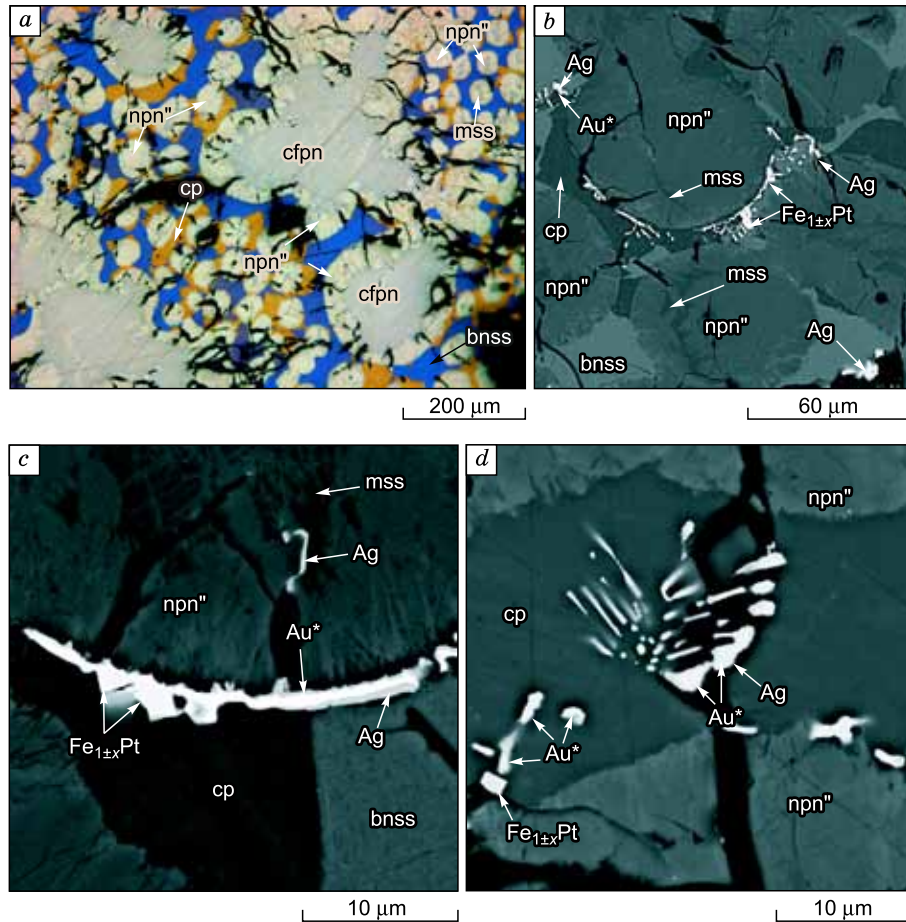
Fig. 7. Microstructures of sulfide minerals and noble metal minerals in zone III. *a*, reflected light image of the three-phase eutectic structure (cfpn + npn + bnss). Large gray iron-copper pentlandite grains correspond to cfpn; light gray small rounded secondary pentlandite grains to npn″; blue bornite solid solution grains to bnss; brown chalcopyrite grains to cp. *b, c, d*, backscattered electrons images; *b*, $Pt_{1+x}Fe|Au^*|Ag$ splices at the npn″/cp interface and Ag inclusions in bnss and at the interface between bnss and npn″; *c*, $Pt_{1+x}Fe|Au^*|Ag$ splice at the npn″/cp and npn″/bnss interfaces; Ag inclusions in npn″; *d*, inclusions of $Pt_{1+x}Fe$, Au*, Ag, and Au*|Ag splices in cp.

the structure gradually transforms into the graphic one towards the end of the zone (Fig. 9*a, b, c*).

As silver solubility in bnss is reduced upon cooling, native Ag inclusions appear in the sulfide. Quaternary solid solution tss decays into npn″ $Fe_{20.8}Ni_{29.5}Cu_{0.9}Pd_{0.3}Ru_{0.3}Ir_{0.4}$ $Rh_{0.7}S_{47.1}$ (Ni/Fe = 1.4), the phase $Me_{11}S_9$ with bulk composition $Fe_{20.5}Ni_{23.1}Cu_{10.9}Pd_{0.2}S_{45.3}$, and mooihoekite mh $Fe_{25.3}$ $Ni_{1.3}Cu_{25.7}S_{47.7}$. The phase $Me_{11}S_9$ decays into npn′ $Fe_{22.7}Ni_{28.7}$ $Cu_{1.2}Pd_{0.2}S_{47.2}$ (Ni/Fe = 1.3) and bnss $Fe_{11.6}Ni_{0.5}Cu_{48.3}S_{39.6}$.

Pt–Fe phases close in composition to tetraferroplatinum $Pt_{1+x}Fe$ and synthetic analog of isoferroplatinum $Pt_{3-x}Fe$, as well as Au* and Ag phases are formed during the melt crystallization.

Elongated $Pt_{1+x}Fe$ grains sized 50 × 5 μm², small faceted crystals, and splices with Au* and Ag are present in npn′ and $Me_{11}S_9$ (Fig. 9*g*). Rectangular and square faceted $Pt_{3-x}Fe$ crystals with sizes from 30 × 20 to 100 × 100 μm² form clusters in the bnss matrix (Fig. 9*d, e, f*), while unfaceted inclusion are present at bnss|npn′ and bnss|$Me_{11}S_9$ interfac-

es. Splices Au*|Ag are associated with boundaries of $Pt_{3-x}Fe$ crystals or npn′ grains or are present in bnss grains (Fig. 9*e–i*). It is also where elongated Ag inclusions are observed (Fig. 9*d*). $Pt_{1+x}Fe$ includes Ni, Cu, Pd, Ir, Ru, Au, and Ag, impurities; $Pt_{3-x}Fe$ includes Ni, Cu, Pd, Ir, Au; Au* includes Cu, Ag, and Pd; and Ag includes Te (Table 2).

Zone V (0.72 ≤ g ≤ 0.82). The scheme of collective behavior of macroelements and noble metal impurities in zone V is shown in Fig. 10. The ingot with bulk composition $Fe_{17.7}$ $Ni_{15.3}Cu_{23.0}Pd_{0.2}Rh_{0.1}S_{43.7}$ (Table 1) is formed in this zone. The melt is depleted in Cu, Fe, and S and enriched in nickel during crystallization. Averages distribution coefficients of Pd, Rh, and Ag between the ingot and the melt are ~ 0.4. Pt, Au, Ru, Ir, and Te contents in the ingot are below the detection limit. The cotectic melt crystallized from the melt consists of bnss $Fe_{12.1}Ni_{0.4}Cu_{47.4}S_{40.1}$ and cnpn $Fe_{22.3}Ni_{24.8}Cu_{5.6}$ $Pd_{0.3}Ru_{0.2}Ir_{0.2}Rh_{0.2}S_{46.4}$ (Ni/Fe = 1.1). The decay of cnpn leads to formation of $Me_{11}S_9$ with composition $Fe_{21.6}Ni_{20.8}$ $Cu_{12.1}Pd_{0.3}S_{45.2}$ and two types of npn, one of them only in-
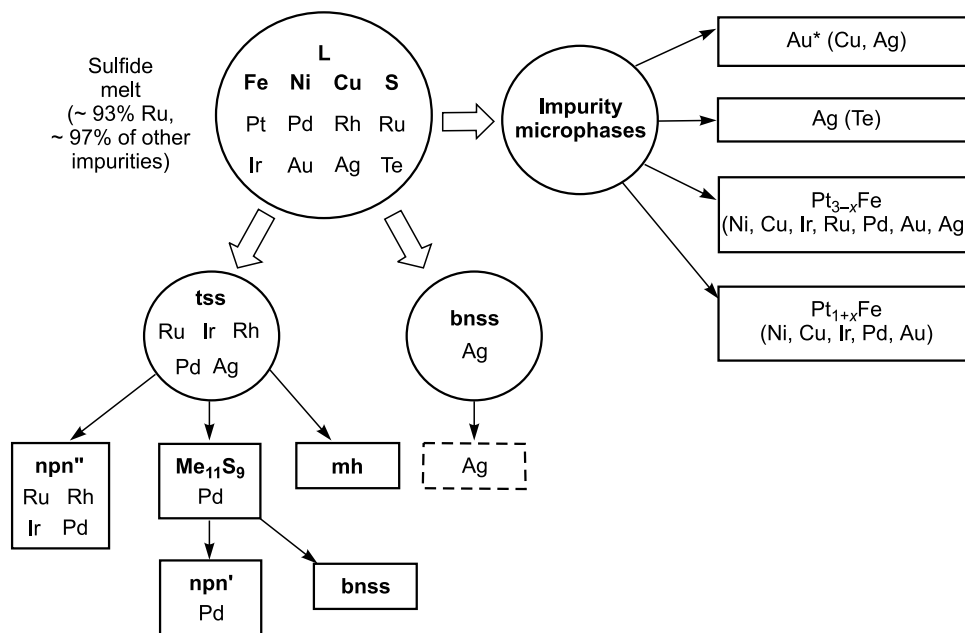
Fig. 8. Crystallization scheme of ore-forming minerals with their further decay in zone IV and noble metal and tellur impurity behavior in these processes. Symbols of complete phase decay products are enclosed in solid rectangles, and silver isolated from bnss upon cooling in dashed rectangles.

cluding Pd impurity (npn′ $Fe_{23.3}Ni_{28.2}Cu_{1.1}Pd_{0.4}S_{47.0}$ (Ni/Fe = 1.2), and another including Pd, Ru, Ir, and Rh (npn″ $Fe_{21.9}Ni_{27.0}Cu_{1.6}Pd_{0.3}Ru_{0.6}Ir_{0.7}Rh_{0.6}S_{47.3}$, Ni/Fe = 1.2) (Fig. 11a). The decay of $Me_{11}S_9$ leads to formation of npn′ with Pd impurity ($Fe_{23.7}Ni_{27.9}Cu_{1.2}Pd_{0.4}S_{46.8}$, Ni/Fe = 1.2) and bnss with composition $Fe_{11.8}Ni_{0.3}Cu_{47.9}S_{40.0}$ (Fig. 11b, c, d, e, g).

Individual crystals of Ag, Au*, $Pt_{3\pm x}Fe_2$, $Pt_{1+x}Fe$, Pt-Fe-Au alloy, as well as their splices, mostly associated with cnpn (Fig. 11b) are crystallized from the melt. $Pt_{3\pm x}Fe_2$ forms rectangular crystals with sizes from 20 × 25 to 35 × 45 μm, with some faces having rough edges. In addition, splices of elongated sharp crystals $Pt_{3\pm x}Fe_2$ with sizes about 5 × 50 μm², dendrites, small crystals with sizes from 1.5 × 1.5 to 5 × 5 μm² spliced with Au* and Ag are observed (Fig. 11c, d, e). Pd, Ir, Au, Cu, Ni, and Te are dissolved in $Pt_{3\pm x}Fe_2$ (Table 2). Small crystals $Pt_{1+x}Fe$ with sizes about 2 μm are present in the splices with Au* and form clusters in npn′ grains (Fig. 11h). Pd, Ir, Cu, and Ni are dissolved in $Pt_{1+x}Fe$ (Table 2). Grains of the solid solution Pt–Fe–Au are associated with $Me_{11}S_9$ and npn′ (Fig. 11f). The bulk composition analysis showed the Au content of about 17 mol.%. The solid solution decays upon temperature decrease into the matrix phase with composition $Pt_{3-x}Fe_2$ and Au* inclusions (Fig. 11f, Table 2). Au* alloy is present in the splices Au*|Ag, $Pt_{1+x}Fe$|Au* and $Pt_{3\pm x}Fe_2$|Au*|Ag (Fig. 11c, d, e). Elongated curved rough splices Au*|Ag are located inside $Me_{11}S_9$ and npn′ grains or at the interface between $Me_{11}S_9$ and bnss (Fig. 11g). Silver in the form of single-phase clumped grains with sizes up to 20 × 15 μm² and elongated inclusions is present in the bnss matrix and the cracks (Fig. 11c, h).

Zone VI (0.82 ≤ g ≤ ~ 1). Formation of the main sulfide phases and impurity behavior in zone VI are illustrated schematically in Fig. 12. The ingot with bulk composition $Fe_{16.7}Ni_{22.6-23.3}Cu_{14.8-15.6}Ag_{0.3}Pd_{0.4}Rh_{0.2}S_{47.3}$ is formed as a result of solidification of the Ni-rich sulfide melt with suspended microdrops similar in composition to Pd_3Te with sizes from < 0.05 to 10 μm. The cotectic alloy crystallized from the sulfide melt consists of bnss $Cu_{51.5}Fe_{9.1}Ni_{0.3}Ag_{0.1}S_{39.0}$ and npn with PGE impurities (Fig. 13a). Two types of pentlandite, namely npn′ and npn″, are formed as a result of npn segregation, one of them only including Pd impurity ($Fe_{20.1}Ni_{31.9}Cu_{0.7}Pd_{0.5}S_{46.8}$, Ni/Fe = 1.6), and another including Pd, Ru, Ir, Rh ($Fe_{18.4}Ni_{31.9}Cu_{0.5}Pd_{0.2}Ru_{0.4}Ir_{0.5}Rh_{1.2}S_{46.9}$, (Ni/Fe = 1.7). Gray nonuniform fragments with bulk composition Cu_5FeS_4, which matches the stoichiometric bnss, and light gray nonuniform fragments with composition $Cu_{5.4}Fe_{0.8}S_{3.8}$ corresponding to nonstoichiometric bnss are formed in bnss upon temperature decrease (Fig. 13d, e, g, h).

Individual crystals of Ag, Au*, Pt_3Fe_2, as well as their splices are formed from the melt. The phase Pt_3Fe_2 is isolated in the form of single crystals, dendrites, and Pt_3Fe_2|Au* and Pt_3Fe_2|Au*|Ag splices forming colonies in the bnss matrix. Au* inclusions are present in some Pt_3Fe_2 grains and crystals (Fig. 13d). In addition to the splices, silver in bnss forms single-phase inclusions (Fig. 13b, d, e). Cu, Ni, Ir, Pd, Ru, and Ag impurities are dissolved in the Pt_3Fe_2 alloy; Ag, Cu, Pd, and Te in Au*; Cu, Fe, and Te in silver (Table 2).

The melt drops based on Pd_3Te with Pt, Au, and Ag impurities are trapped by npn and solidify in the form of globular multiphase inclusions upon cooling of the ingot (Fig. 13b–h). Similar inclusions were discovered in both
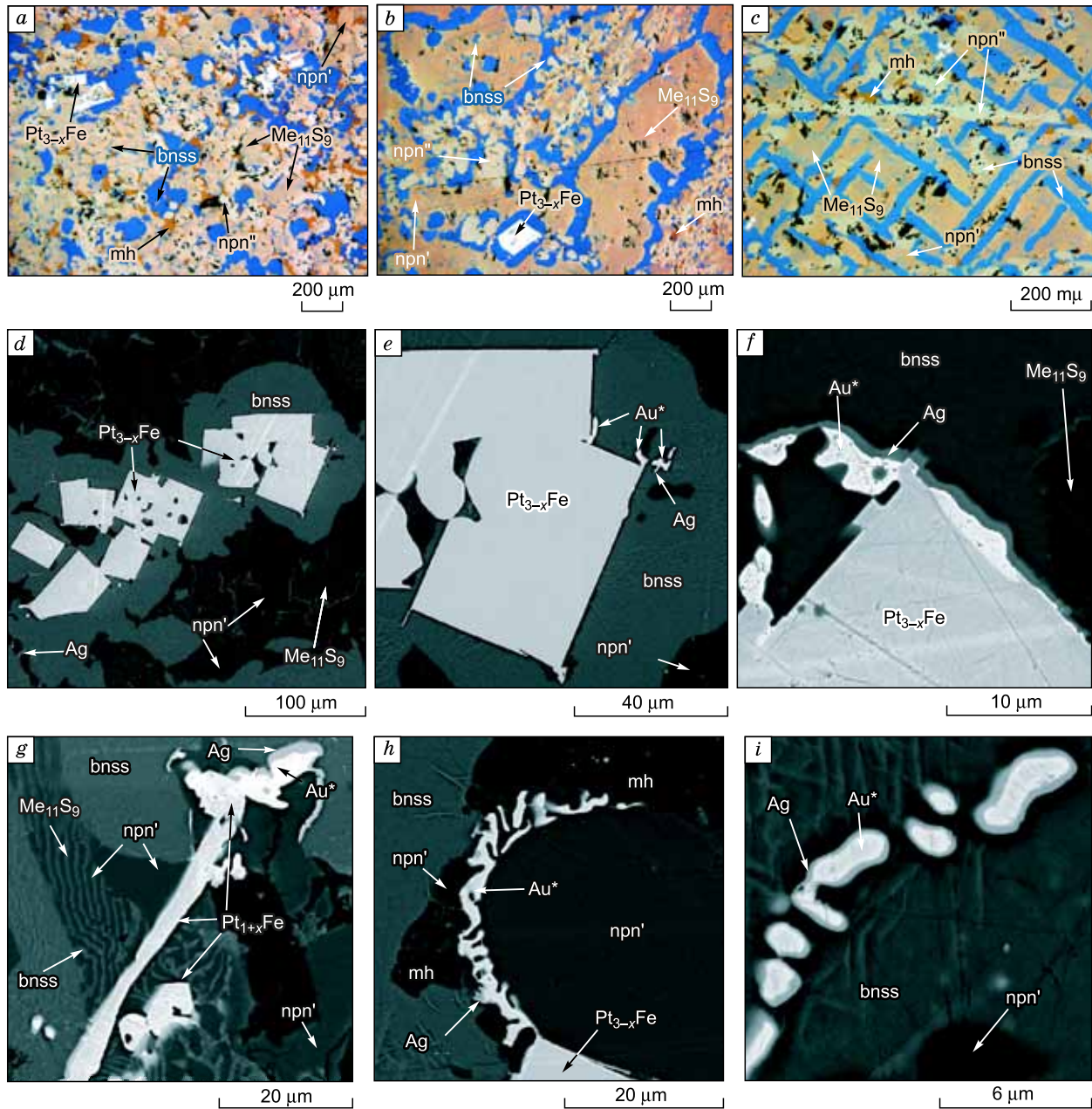
Fig. 9. Microstructures of the main ore-forming minerals and noble metal microminerals in zone IV. Reflected light microimages illustrate the evolution of microstructures of the main ore-forming minerals along the zone, (*a*) g = 0.2, (*b*) g = 0.6, (*c*) g = 0.7. Microstructures for microminerals are imaged in backscattered electrons (*d–i*). See the notes in the text.

natural and synthetic sulfides (Barnes et al., 2006; Helmy et al., 2007; Cafagna and Jugo, 2016). Their appearance is associated with the segregation of the sulfide melt, which includes Te impurity along with other metalloids, into the sulfide and predominantly telluride melts at temperatures of 825–725 °C. The bulk composition of the telluride melt (mol.%) is as follows: Te ∼ 57, Pd ∼ 22, Ag ∼ 7, Au ∼ 4, Cu ∼ 4, and Pt, Fe, Ni with contents of ∼2 each. Solidified inclusions mostly consist of the phase $Pd_{3-x}Te$ with Ag im-

purity (Table 2). Small (≤ 1 μm) spherical globules and non-spherical microphase inclusions containing Pt, Au, and Ag, whose composition we were unable to precisely identify, are present in the phase matrix (Fig. 13*f, h*).

The obtained results allow us to assume the possibility of formation of Te- and Pd-rich liquid (L–Te) microdrops with Pt, Au, and Ag impurities suspended in the sulfide melt. The sulfide cotectics (npn + bnss) are crystallized upon temperature decrease, and L–Te microdrops are trapped by the pent-
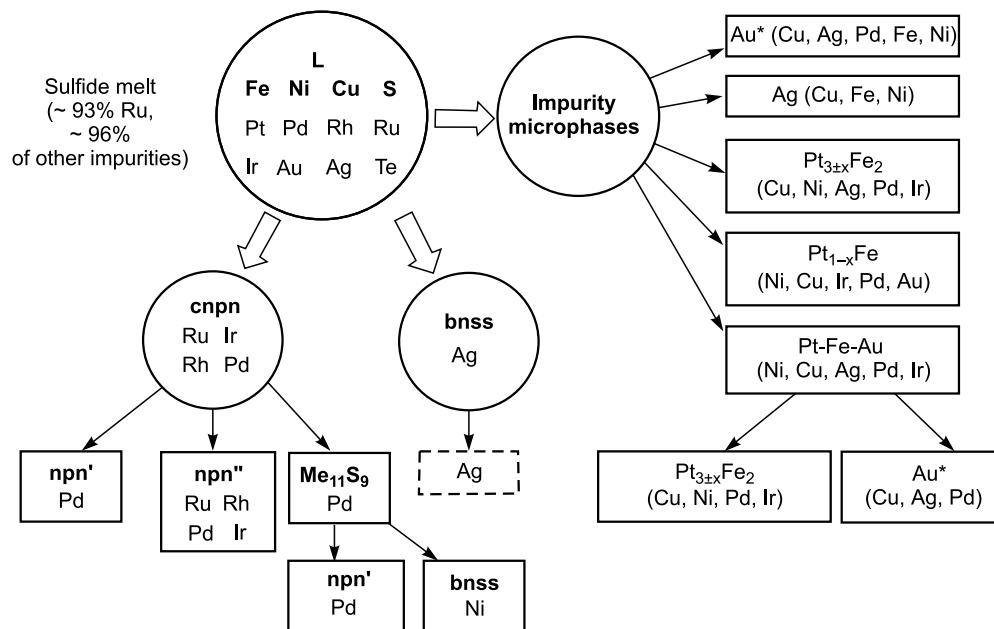
Fig. 10. Crystallization scheme of ore-forming minerals with their further decay in zone V and noble metal and tellur impurity behavior in these processes. See Fig. 8 for symbol keys.

landite phase. As L–Te solidifies, the Pd_3Te matrix with Ag impurity is formed, in which noble metal microphase inclusions, such as Pt, Au, and Ag, are crystallized.

DISCUSSION

Formation of the primary impurity zoning

Solid solutions of trace elements. During the melt crystallization, impurities may either be transferred into the solid ingot in the form of solid solutions in the primary main minerals or may form autonomous mineral inclusions. In the first case, the classical impurity distribution between the liquid and the solid phase is implemented and characterized by average distribution coefficient values (κ). The Pd distribution curve along the crystallized sample and the calculated changes in Pd contents in the melt are shown in Fig. 14 to illustrate this case. Similarly to the macrocomponents, its concentration changes smoothly within the zones and abruptly between the zones. We can see $\kappa < 1$ at all crystallization stages, i.e., Pd progressively accumulates in the melt as the sample solidifies. The zonal behavior of the impurity is clearly demonstrated in Fig. 14.

It can be seen from Tables 1, 2 and schemes in Figs. 2, 4, 6, 8, 10, and 12 that impurities are mostly concentrated in the primary pentlandites and tss, aside from zone II, where we were only able to chemically identify Ag and Pd. The bnss phase acts as the main Ag concentrator.

High-temperature solid solution tss and pentlandites are identified by composition and visually distinctive features in microimages. According to the literature, tss has a vast metal element homogeneity area and includes 44.8 to 46.1 mol.% S (Peregoedova et al., 1995). The tss phase in our experi-

ment contains: $x_S \sim 45.5$ mol.%, Fe/Ni = 1.1, Cu $\approx$ 10–13 mol.%. The tss phase is formed in zone IV by the reaction L + cfpn = bnss + tss (Kosyakov and Sinyakova, 2017a). It also dissolves Rh, Ru, Ir, and Pd.

Phases with sulfur contents of 46.5 to 47.4 mol.%, i.e., $\sum Me/S$ from 9.1/7.9 to 9/8 are discovered in the experiment. These phases are close in their compositions to the stoichiometric pentlandite Me_9S_8. It should be noted that $\sum Me/S$ for pentlandite in the system Fe–Ni–S varies from 8.9/8.1 to 9.2/7.8 (Sinyakova and Kosyakov, 2001). According to the schemes (Figs. 2, 4, 6, 8, 10, and 12), cfpn (zones I–III), cnpn (V), and npn (zones III and VI) with differing metal element ratios are the primary pentlandite phases.

The cfpn phase in zones I and III shows Ni / Fe = 0.7–0.8, and $x_{Cu} \sim 8$ mol.%. In zone I, cfpn is most likely crystallized from the melt via the reaction L = cfpn at 850 °C. In zone III, it is a part of the triple cotectics formed via the reaction L = bnss + cfpn + npn. Regardless of the formation reaction, it includes Rh, Ir, and Ru impurities in quantities of 0.4–0.6 mol.% each. The second type of this pentlandite referred to as cfpn* is crystallized from the melt in zone II via the reaction L = bnss + cfpn*. This phase includes 11 mol.% Cu and Pd impurity. The remaining PGE contents were below the analytical error.

Pentlandite cnpn is moderately nickeliferous (Ni/Fe = 1.1) and includes 5.6 mol.% Cu. It is formed in zone V via the reaction L + tss = cnpn + bnss. Pd (0.3 mol.%), Rh, Ir, and Ru (0.2 mol.% each) are dissolved in the cnpn phase.

Ni-rich pentlandite npn is crystallized from the sulfide melt in zones III and VI. The melt at the beginning of zone III contains 19.4 mol.% Ni and 16.9 mol.% Cu, while npn is formed via the cotectic reaction L = npn + cfpn + bnss.
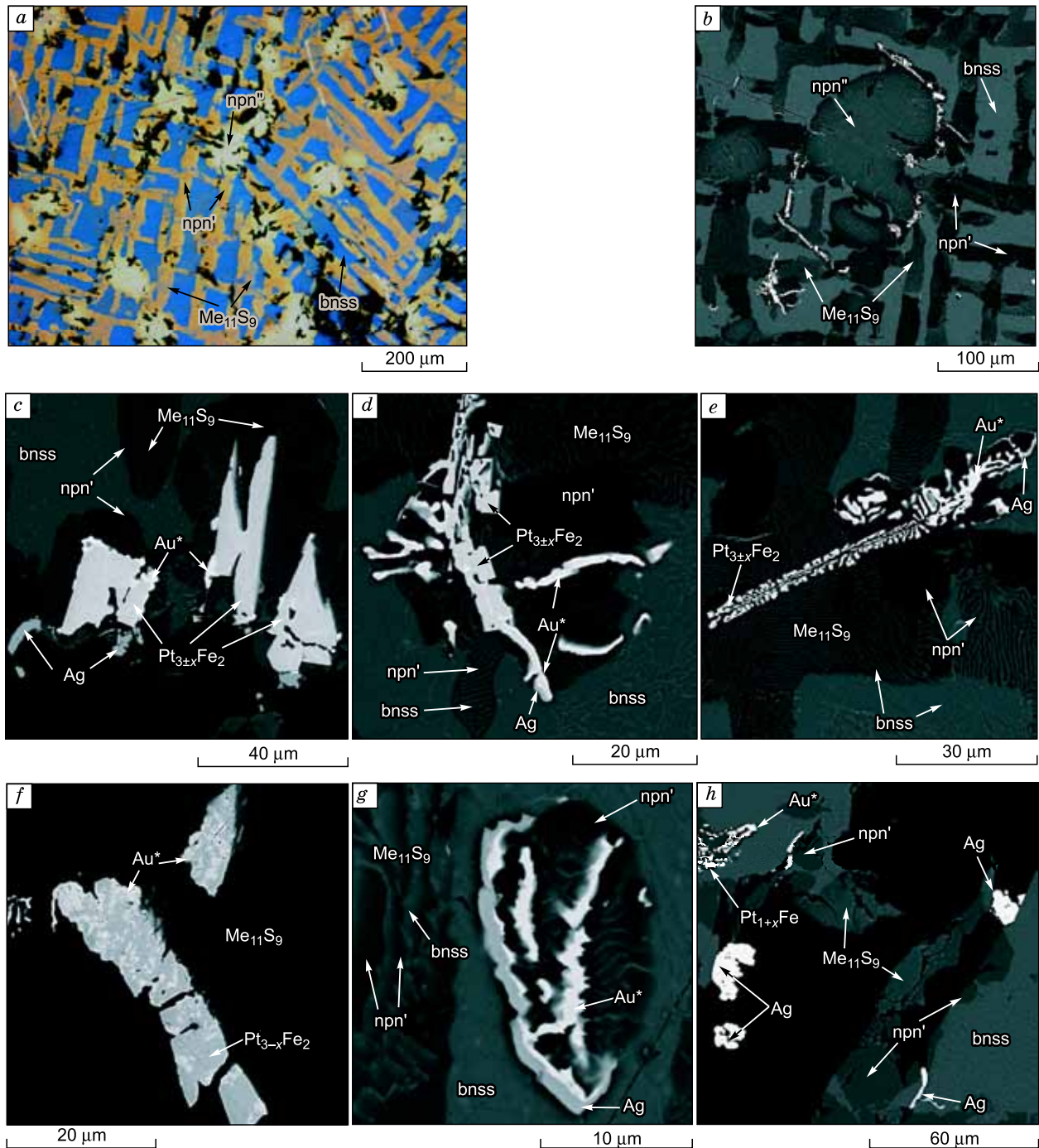
Fig. 11. Peculiar microstructures for the main ore-forming minerals and noble metal microminerals in zone V. *a*, Reflected light image; *b–h*, electron microscope images. See the notes in the text.

It is characterized by the ratio Ni / Fe = 1.2 and includes 1.6 mol.% Cu. In zone VI, npn is crystallized from the melt enriched in nickel (23.8 mol.%) and depleted in Cu (10.6 mol.%). Thus, it is enriched in Ni (Ni/Fe = 1.6) and depleted in Cu (0.6 mol.%). Despite the significant difference in macrocomponent contents, we assumed that both these pentlandites represent the same phase since they dissolve the same impurities, specifically Pd, Rh, Ir, and Ru.

Noble metal microphases. The presence of various microphases in specific zones is shown in Table 3. We can see that these phases are deposited from the melt at various melt solidification stages. Ruthenium is mostly crystallized from the melt in the form of refractory compound RuS_2 at the very beginning of the solidification process. The formation condition of autonomous crystals from the melt may be written down as $a_{Ru}a^2_S \geq SP_{RuS_2}$, where a is the activity and

Table 3. Microphases present in the primary zones of the crystallized sample

Mineral	Formula	T_m, °C	Crystallized melt fraction (g)											
			0.004	0.08	0.10	0.20	0.30	0.40	0.50	0.60	0.72	0.82	0.90	1.0
			I	II	III	IV						V	VI	
Laurite	RuS_2	~1600	+	–	–	–	–	–	–	–	–	–	–	–
Tetraferroplatinum	$Pt_{1\pm x}Fe$	~1300	–	+	+	+	+	+	+	+	+	+	–	–
Isoferroplatinum	$Pt_{3-x}Fe$	~1350	–	–	–	+	+	+	+	+	+	–	–	-
Pt_3Fe_2	Pt_3Fe_2	~1320*	–	–	–	–	–	–	–	–	–	+	+	+
Pt–Fe–Au solid solution	Pt–Fe–Au		–	–	–	–	–	–	–	–	–	+	+	+
Gold-based alloy	Au*	< 1063	–	+	+	+	+	+	+	+	+	+	+	+
Silver	Ag	960	–	+	+	+	+	+	+	+	+	+	+	+
Keithconnite	$Pd_{3-x}Te$	~780	–	–	–	–	–	–	–	–	–	–	+	+

Note. I–VI, primary zone numbers; the plus signs indicate the cases, when various phases were observed.
*Subsolidus formation temperature.

SP is the solubility product. Despite the low ruthenium content in the initial melt, this condition is most likely to hold at $T \sim 850$ °C, which corresponds to the beginning of the melt crystallization in our experiment. It is indicated by large RuS_2 crystal sizes and their clearly visible faceting. Ag is the only single-element phase with the impurity content not exceeding ~ 6 mol.%. Au* phase contains up to 22 mol.% of Ag, Cu, and Pd impurities, which agrees with the structure of liquid-solid diagrams Au–Ag, Au–Cu, Au–Pd, Au–Ag–Cu, and Au–Ag–Pd (Massalski et al., 1990; Effenberg and Ilyenko, 2006). Pt–Fe phases close in their composition to tetraferroplatinum $Pt_{1\pm x}Fe$ and isoferroplatinum $Pt_{3-x}Fe$ are present in the sample, along with the $Pt_{3\pm x}Fe_2$ phase. Non-stoichiometric compounds PtFe, Pt_3Fe, and $PtFe_3$ with wide

homogeneity areas forming as a result of decay of the continuous solid solution at $T \sim 1300$, 1350, and 820 °C, respectively, are present in the Pt–Fe phase diagram (Massalski et al., 1990). Pt_3Fe_2 compound is absent from the diagram. The nugget with composition ~ Pt_3Fe_2 is mentioned in the paper by T.L. Evstigneeva (2009) dedicated to the investigation of natural Pt–Fe minerals. Solid solution Pt-Fe-Au containing about 17 mol.% Au is present in zone V. The grains of this phase with sizes up to 15 μm look like products of decay into Pt_3Fe_2 and Au*.

The melt is depleted in Fe during the sample crystallization (Fig. 1), which affects the Pt–Fe phase separation sequence along the sample (Table 3, Figs. 4, 6, 8, 10, and 12). $Pt_{1\pm x}Fe$ is formed in zones II–V, a less iron-rich $Pt_{3\pm x}Fe$ com-
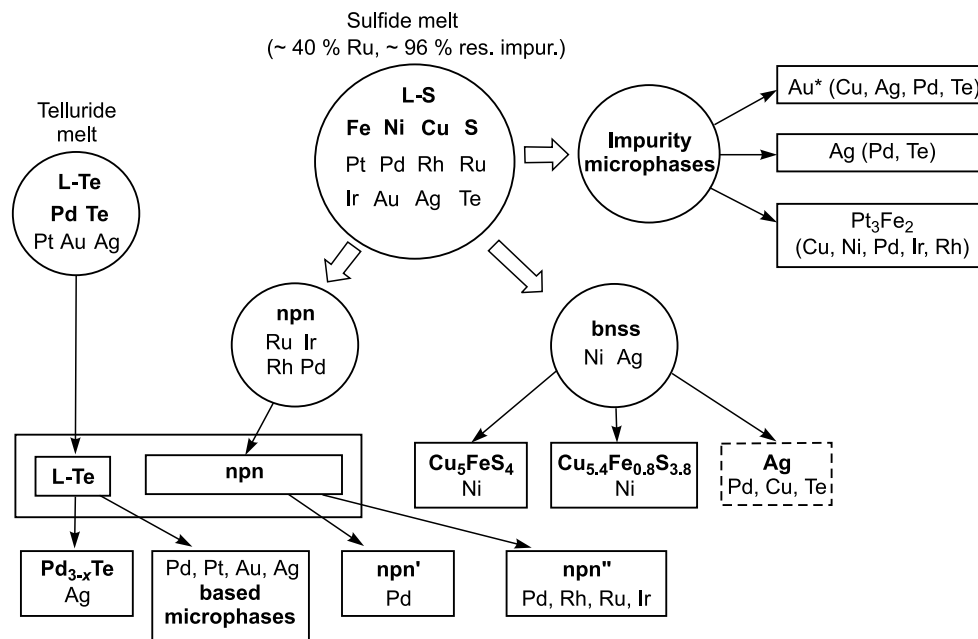

Fig. 12. Crystallization scheme of the sulfide melt in zone VI and impurity behavior in this process. Symbols of complete phase decay products are enclosed in solid rectangles, and impurities isolated from bnss upon cooling in dashed rectangles.
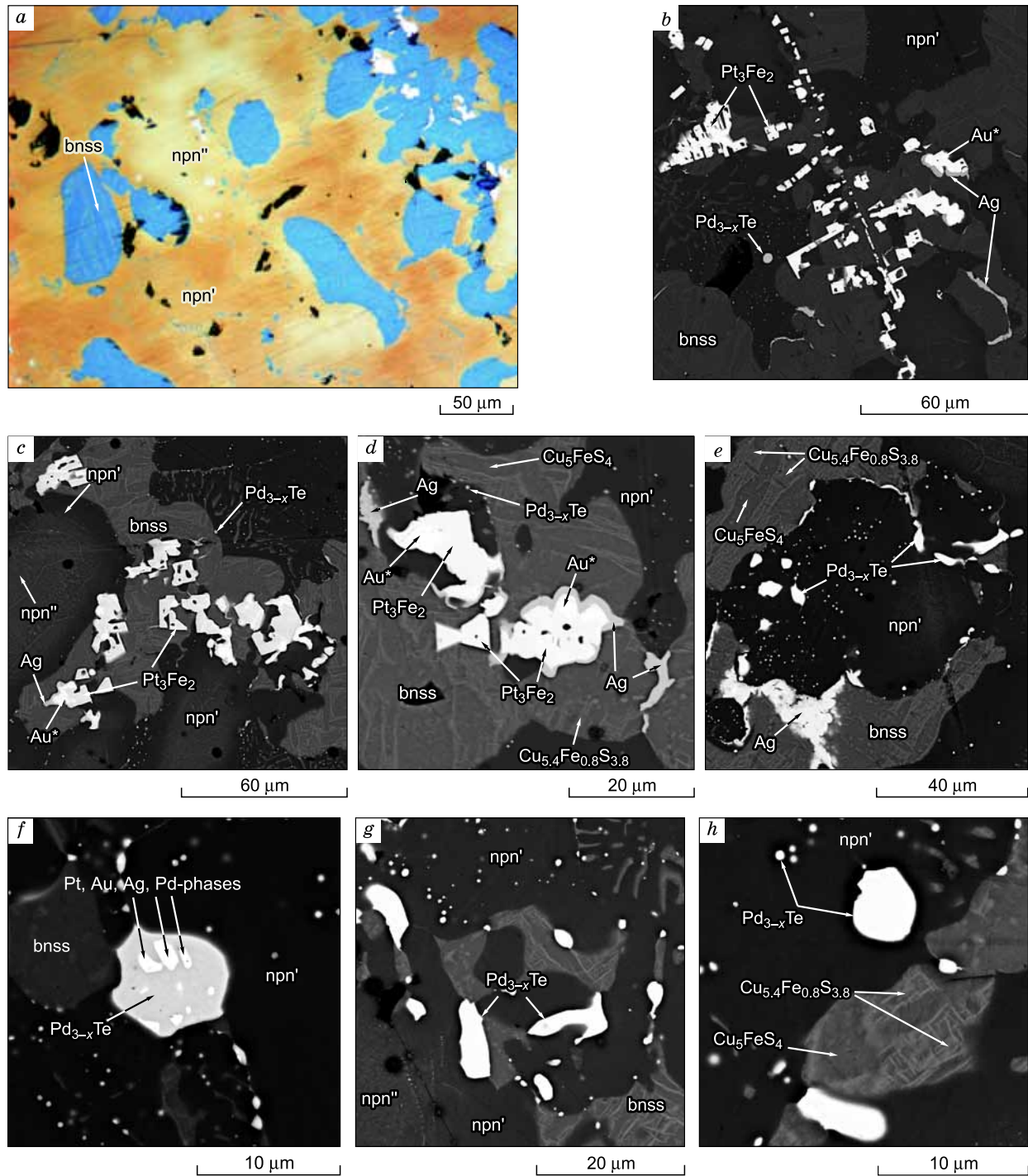
Fig. 13. Microstructures of the main ore-forming minerals and noble metal microminerals in zone VI. *a*, Reflected light image; *b–h*, electron microscope images. See the notes in the text.

pound appears in zone IV, the phase with composition $Pt_{3\pm x}Fe_2$ is formed in zones V–VI, and solid solution Pt–Fe–Au is additionally formed in zone V. It should be noted that Pt–Fe phases can dissolve Cu, Ni, Ir, Ru, Pd, Au, and Ag. Impurities may show intricate behavior during the zonal sample crystallization (Figs. 4, 6, 8, 10, and 12). For example, Rh is present in zones I and VI, which is associated with

the fact that rhodium is mostly concentrated in zone I as an impurity in RuS_2, while the remaining Rh only accumulates significantly in the melt in zone VI, where it is present in $Pt_{3\pm x}Fe_2$.

Primary microphase distribution regularities along the sample. According to the theory, formation of a new macro- or microphase should be matched with the appear-
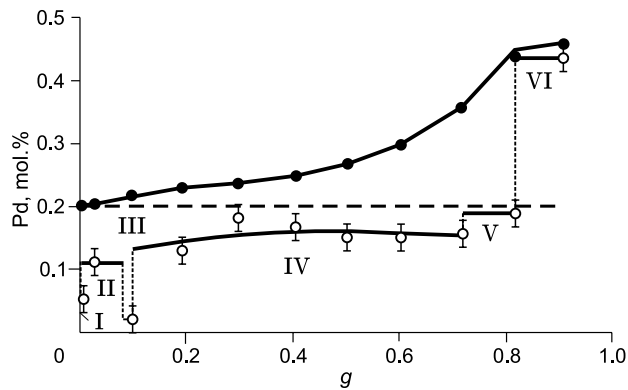
Fig. 14. Changes in average Pd content in the ingot (light circles) and the melt (dark circles) during crystallization. Dashed horizontal line indicates Pd content in the initial melt. I–VI, ingot primary zones separated by dashed vertical lines.

ance of a new impurity zone (Kosyakov and Sinyakova, 2015). It means that impurity phases inside the macrozone are isolated successively. For example, Au*, Ag, and $Pt_{1+x}Fe$ are present in zone II. Thus, $Pt_{1+x}Fe|Pt_{1+x}Fe + Au*|Pt_{1+x}Fe + Au* + Ag$ should be present in this zone in the quasi-equilibrium approximation. In reality, however, the presence of these minerals is observed throughout the whole length of zone II, which means that, contrary to macrocomponents, trace elements are crystallized in nonequilibrium mode. It may be attributed to the following circumstance. Macrophases form a single crystallization front during the fractional solidification of the melt. Microphases, however, are unable to form a continuous interface between the crystals and the melt due to small impurity contents in the melt. Therefore, they are formed as a result of nuclei formation near the crystallization front and their further growth. Nucleation process occurs under strongly nonequilibrium conditions, which defines the observed impurity zoning peculiarities.

Ru, Pt, Au, and Ag microphases are present in the main sulfide mineral matrix in the form of single-phase, two-phase, and three-phase splices. They form isolated inclusions located in the inner parts of the main sulfide grains or at intergrain boundaries. Micromineral splice formation is a distinctive feature of the process. According to the data obtained, laurite RuS_2 and Pt–Fe–Au solid solution form single crystals (Figs. 3, 11*f*). Two-phase and three-phase splices are formed by the following microminerals: $Pt_{1\pm x}Fe|Au*$, $Pt_{1\pm x}Fe|Ag$, $Pt_{3-x}Fe|Au*$, $Pt_{3-x}Fe|Ag$, $Pt_3Fe_2|Au*$, $Au*|Ag$, $Pt_{1\pm x}Fe|Au*|Ag$, $Pt_{3-x}Fe|Au*|Ag$, $Pt_3Fe_2|Au*|Ag$. In our opinion, splice formation may be explained by the fact that nuclei of the less soluble phases are formed in the melt first, and then nuclei of more soluble phases arise at their surfaces.

Telluride melt crystallization. Tellur is concentrated in the sulfide melt during crystallization in zones I–VI. Its concentration in the melt in zone VI is 1.8 mol.%, which is enough to form drops with sizes up to 10 μm including ~25 mol.% Te. Under these circumstances, Te-melt nuclei formation, growth, and coagulation occur. Under specific

conditions, the drops are trapped by the crystallizing pentlandite grains with formation of spherical or elongated inclusions. The matrix with composition $Pd_{3-x}Te$ with a small number of small microphase inclusions of the system Au–Pt–Ag is formed during the solidification of drop-like inclusions in zone VI. According to (Okamoto, 2004), Pd_3Te compound, which is formed at 785 °C via the peritectic reaction $L + Pd_8Te_3 = Pd_3Te$ and decays at 727 °C via the reaction $Pd_3Te = Pd_{17}Te_4 + Pd_{20}Te_7$, is present in the system Pd–Te. In our case, it seems to be this phase that is formed from the telluride melt drops, however, it does not decay upon cooling. It may be considered as a synthetic analogue of keithconnite mineral $Pd_{3-x}Te$ (0.14 < *x* < 0.43) (Cabri et al., 1979; Cabri, 2002). It was found in association with noble metal microminerals Pd–Au–Cu, Pt–Fe, Au–Ag alloys, $PtAs_2$, etc. in bornite-digenite and bornite-chalcopyrite sulfide globules in the Platinova Reef in the Skaergaard intrusion, eastern Greenland, which is an example of a magmatic Cu–PGE–Au sulfide deposit formed at late stages of magmatic differentiation (Holwell et al., 2015).

Formation of the secondary impurity zoning

Solid-phase reactions occur in the crystallized sample upon its cooling, which leads to changes in both the main and impurity zoning of the sample. Formation of the secondary impurity zoning is firstly associated with complete and partial decay of the primary macro- and microphases and secondly with impurity redistribution during solid-phase reactions.

Inclusions of the primary solid solution Pt–Fe–Au completely decay in our sample into the mixture of secondary microphases $Pt_{3-x}Fe_2$ and Au* (Fig. 11*f*). Partial decay of the parent phases with formation of the daughter microphases occurs as a result of decreasing impurity solubility in them. Thus, Ag inclusions appear in the bornite solid solution bnss (Figs. 11*h*, 13*b*, *d*, *e*) and Au* in the primary Pt–Fe minerals $Pt_{1\pm x}Fe$ (Fig. 5*c*) and Pt_3Fe_2 (Fig. 13*d*).

Consider the main behavior features of impurities during solid-phase processes involving pentlandites and tss. When these primary minerals are cooled, solid-phase reactions occur with formation of secondary pentlandites. The lack of experimental data and multistage nature of the decay process make it impossible to fully describe it as a phase reaction sequence. These pentlandites are also identified based on the main and impurity compositions, as well as visually distinctive features in microimages (color, morphology, grain sizes, etc.). Ni-rich low-temperature pentlandites referred to as npn′ and npn″ act as the main impurity concentrators. They are close in contents of the main components but differ significantly in their PGE accumulation ability. The npn′ phase only shows Pd impurity content within the analytical error, while the npn″ phase simultaneously dissolves Pd, Ru, Ir, and Rh. It is possible that structures of these phases are similar in general, but different in detail. These phases were formed from cfpn, cnpn, npn, and tss as a result of solid-phase reaction chains that occur upon tem-
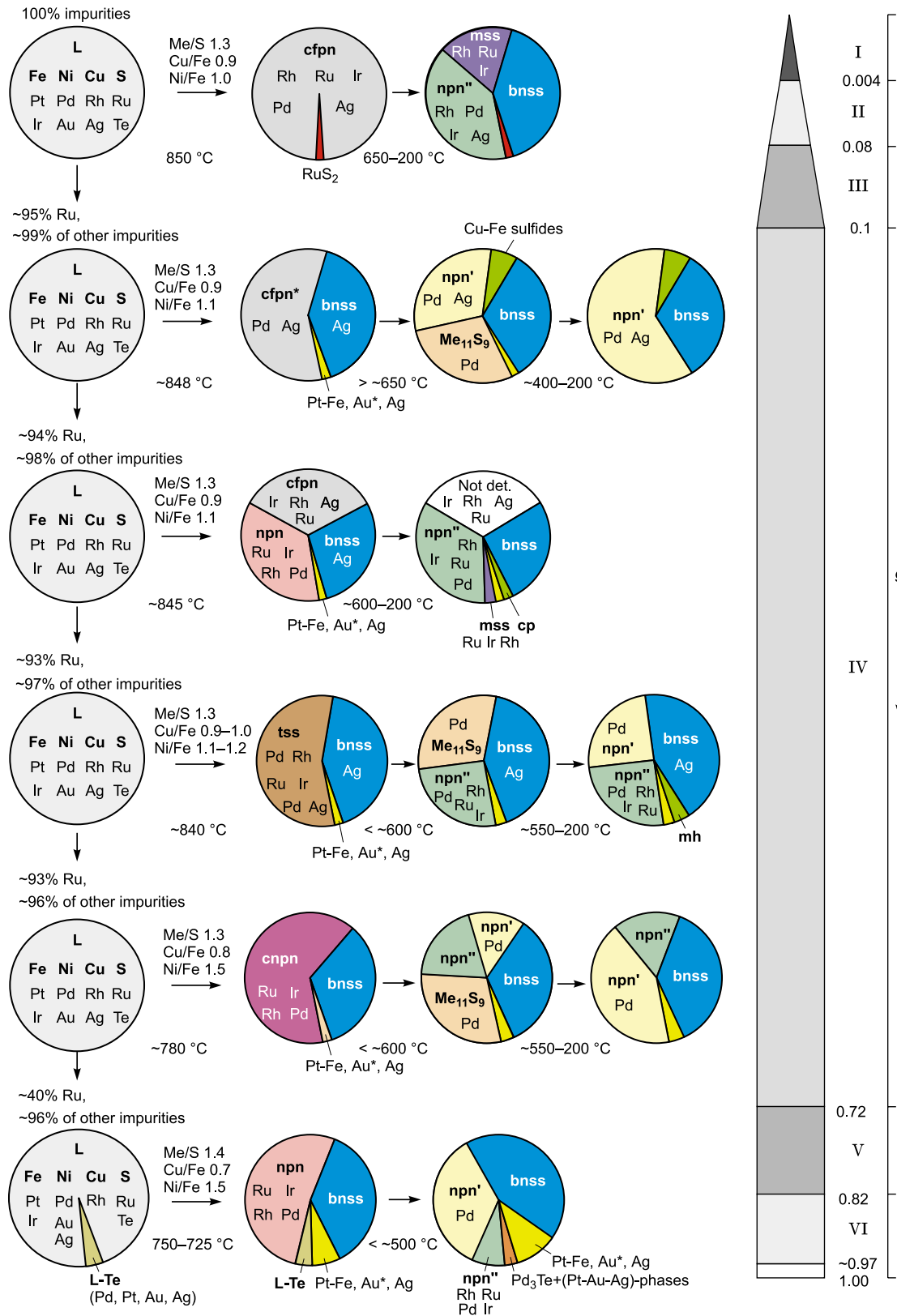
Fig. 15. Schematic illustration of zonal structure of the crystallized ingot and phase composition evolution during fractional crystallization. L, sulfide melt, L–Te–telluride melt. Primary pentlandites: cfpn and cfpn*, enriched in iron and copper, cnpn, moderately nickeliferous with ~ 6 mol.% Cu, npn, Ni-rich, bnss, primary and secondary bornite solid solution. Secondary phases: pentlandite npn′ (Pd impurity), pentlandite npn″ (Pd, Ru, Ir, and Rh impurities), mss, monosulfide solid solution enriched in Fe, Fe–Cu sulfides, chalcopyrite, haycockite, mooihoekite, talnakhite. Microphases of RuS_2, Au*, Ag, Pd_3Te, and alloys of the systems Pt–Fe and Pt–Au–Ag.

perature decrease (Figs. 2, 4, 6, 8, 10, and 12). The npn′ phase is a decay product of cfpn in zone II and cnpn in zone V. In addition, npn′ appears as a result of $Me_{11}S_9$ intermediate phase decay presumably via the reaction $Me_{11}S_9$ = npn′ + bnss in zones II, IV, and V (Fig. 5*d*, 9*f*, *g*, 11*b*, *c*, *d*, *e*, *g*, *h*). In zone VI, npn′ is formed via the reaction npn = npn′ + npn″. The npn″ phase is a decay product of cfpn, tss, and cnpn in zones I, IV, and V respectively and is isolated as a result of npn decay in zones III and VI as well.

Generalized evolution scheme of the ingot phase composition during fractional crystallization

Conventional approaches to studying trace element behavior are based on generalization of geochemical data and experimental research of phase relations in systems Cu–Fe–Ni–S–(trace elements). The samples studied in the present paper were obtained as a result of continuous macroelement and impurity fractionation. Here, time evolution is associated with continuous changes in the melt composition during its fractional crystallization. The estimates showed that macrocomponent distribution both in the laboratory experiment and during orebody formation agreed with the quasi-equilibrium directional crystallization model and was primarily defined by the structure of the equilibrium phase diagram, sulfide magma composition, and crystallization trajectory location at the liquidus hypersurface. However, the impurity distribution is defined by more intricate mechanisms. Changes in crystallization temperature are the natural consequence of fractional solidification of sulfide magma. Evolution of local phase and chemical compositions of the crystallized mass results from subsolidus phase processes during its cooling, which definitively forms chemical and phase structure of the experimental sample or the orebody.

Description of the fractional crystallization of sulfide melts with formation of pentlandite-bornite massive orebodies and isolation of autonomous noble metal minerals in presence of nonmetallic elements is unavailable in the literature. The results of the present study have demonstrated the potential for implementing a rather complex fractional crystallization process and made it possible to identify the evolution of macro- and microphase composition of the sample. This evolution is illustrated schematically in Fig. 15. It clearly shows both the primary zoning peculiarities, i.e., macro- and microphase separation sequences during the melt crystallization, and subsolidus processes in each zone, which lead to formation of the secondary main and impurity zoning.

CONCLUSIONS

The use of the experimental results and application of the directional crystallization model to them made it possible to describe the behavior of the 12-component system Cu–Fe–Ni–S–(Pt, Pd, Rh, Ir, Ru, Ag, Au, Te) in this process. It is shown in the present paper that pentlandites and quaternary solid solution tss are the main high-temperature PGE con-

centrators. Thus, taking into account the three primary forms of pentlandite is critical for constructing genetic schemes of PGE fractionation. The Ni-rich pentlandites are the main low-temperature PGE concentrators formed as a result of solid-phase reaction chains. PGE impurities act as indicators of these reactions by manifesting their specific individual and group properties. High-temperature cfpn*, unquenchable intermediate phase $Me_{11}S_9$, and a low-temperature pentlandite phase npn′ only dissolve Pd, while another pentlandite phase npn″ simultaneously concentrates Pd, Ru, Ir, and Rh.

It is shown that noble metal microphases are formed by different mechanisms: (a) crystallization from the sulfide melt of refractory compounds, (b) crystallization from the immiscible telluride melt, and (c) formation through complete or partial decay of primary macro- and microphases.

Our data on the effect that tellur has on PGE behavior agree with the studies of experimental and natural samples (Barnes et al., 2006; Helmy et al., 2007; Holwell and McDonald, 2007; Cafagna and Jugo, 2016), which show evidence of sulfide-telluride melt separation in the form of telluride inclusions with Pd, Pt, Au, and Ag impurities in the sulfide matrix. It should be noted that the studied sample shows the presence of telluride inclusions in the pentlandite matrix.

REFERENCES

Ballhaus, C., Tredoux, M., Spath, A., 2001. Phase relations in the Fe–Ni–Cu–PGE–S system at magmatic temperature and application to massive sulphide ores of the Sudbury igneous complex. Petrology 42 (10), 1911–1926.

Barnes, S.-J., Cox, R.A., Zientek, M.L., 2006. Platinum-group element, gold, silver and base metal distribution in compositionally zoned sulfide droplets from the Medvezky Creek mine, Noril'sk, Russia. Contrib. Miner. Petrol. 152 (2), 187–200.

Barnes, S.-J., Ripley, E.M., 2016. Highly siderophile and strongly chalcophile elements in magmatic ore deposits. Rev. Miner. Geochem. 81 (1), 725–774.

Cabri, L.J., 2002. The Platinum-Group Minerals, in: Cabri, L.J. (Ed.), The Geology, Geochemistry, Mineralogy and Mineral Beneficiation of Platinum-Group Elements. Can. Inst. Mining, Metallurgy and Petroleum, Spec. Vol. 54, pp. 13–129.

Cabri, J., Rowland, J.F., Laflamme, J.H.G., Stewart, J.M., 1979. Keithconnite, telluropalladinite and other Pd–Pt tellurides from the Stillwater Complex, Montana. Can. Mineral. 17 (3), 589–594.

Cafagna, F., Jugo, P.J., 2016. An experimental study on the geochemical behavior of highly siderophile elements (HSE) and metalloids (As, Se, Sb, Te, Bi) in a mss–iss–pyrite system at 650 ºC: a possible magmatic origin for Co–HSE-bearing pyrite and the role of metalloid-rich phases in the fractionation of HSE. Geochim. Cosmochim. Acta 178, 233–258.

Craig, J.R., Kullerud, G., 1969. Phase relations in the Cu–Fe–Ni–S system and their application to magmatic ore deposits, in: Wilson. H.D.B. (Ed.), Magmatic Ore Deposits. Soc. Explor. Geophysic., Geophys. Monogr. Ser., Vol. 4, pp. 344–358.

Czamanske, G.K., Kunilov, V.E., Zientek, M.L., Cabri, L.J., Likchachev, A.P., Calk, L.C., Oscarson, R., 1992. A proton microprobe study of magmatic sulfide ores from the Noril'sk-Talnakh district, Siberia. Can. Mineral. 30 (2), 249–287.

Dare, S.A.S., Barnes, S.-J., Prichard, H.M., Fisher, P.C., 2014. Mineralogy and geochemistry of Cu-rich ores from the McCreedy East Ni–Cu–PGE deposit (Sudbury, Canada): Implications for the behavior of platinum group and chalcophile elements at the end of crystallization of a sulfide liquid. Econ. Geol. 109 (2), 343–366.

Distler, V.V., Grokhovskaya, T.L., Evstigneeva, T.L., Sluzhenikin, S.F., Filimonova, A.A., Dyuzhikov, O.F., Laputina, I.P., 1988. Petrology of the Magmatic Sulfide Ore Formation [in Russian]. Nauka, Moscow.

Distler, V.V., Sinyakova, E.F., Kosyakov, V.I., 2016. Behavior of noble metals upon fractional crystallization of copper-rich sulfide melts. Dokl. Earth Sci. 469 (2), 811–814.

Duran, C.J., Barnes, S.-J., Pleše, P., Prašek, M.K., Zientek, M.L., Pagé, P., 2017. Fractional crystallization-induced variations in sulfides from the Noril'sk-Talnakh mining district (polar Siberia, Russia). Ore Geol. Rev. 90, 326–351.

Effenberg, S., Ilyenko, S. (Eds.), 2006. Noble Metal Systems. Selected Systems from Ag–Al–Zn to Rh–Ru–Sc. Landolf-Börnstein–Group IV. Phys. Chem. Vol. 11B. Springer-Verlag, Berlin-Heidelberg.

Evstigneeva, T.L., 2009. Phases in the Pt–Fe system. Electron. Sci. Inform. J. Vestnik Otdelenia nauk o Zemle RAN 1 (27). http://www.scgis.ru/russian/cp1251/h_dgggms/1-2009/informbul-1_2009/mineral-6.pdf.

Fleet, M.E., Chryssoulis, S.L., Stone, W.E., Weisener, C.G., 1993. Partitioning of platinum-group elements and Au in the Fe–Ni–Cu–S system: experiments on the fractional crystallization of sulfide melt. Contrib. Mineral. Petrol. 115 (1), 36–44.

Fleet, M.E., Pan, Y., 1994. Fractional crystallization of anhydrous sulfide liquid in the system Fe–Ni–Cu–S, with application to magmatic sulfide deposits. Geochim. Cosmochim. Acta 58 (16), 3369–3377.

Genkin, A.D., Evstigneeva, T.L., 1986. Associations of platinum-group minerals of the Noril'sk cooper-nickel sulfide ores. Econ. Geol. 81 (5), 1203–1212.

Genkin, A.D., Distler, V.V., Gladyshev, G.D., Filimonova, A.A., Evstigneeva, T.L., Kovalenker, V.A., Laputina, I.P., Smirnov, A.V., Grokhovskaya T.L., 1981. Sulfide Copper-Nickel Ores of the Noril'sk Deposits [in Russian]. Nauka, Moscow.

Helmy, H.M., Ballhaus, C., Berndt, J., Bockrath, C., Wohlgemuth-Ueberwasser, C., 2007. Formation of Pt, Pd and Ni tellurides: experiments in sulfide-telluride systems. Contrib. Mineral. Petrol. 153 (5), 557–591.

Helmy, H.M., Ballhaus, C., Wohlgemuth-Ueberwasser, C., Fonseca, R.O.C., Laurenz, V., 2010. Partitioning of Se, As, Sb, Te and Bi between monosulfide solid solution and sulfide melt–application to magmatic sulfide deposits. Geochim. Cosmochim. Acta 74, 6174–6179.

Holwell, D.A., McDonald, I., 2007. Distribution of platinum-group elements in the Platreef at Overysel, northern Bushveld Complex: a combined PGM and LA-ICP-MS study. Contrib. Mineral. Petrol. 154 (2), 171–190.

Holwell, D.A., McDonald, I., 2010. A review of the behavior of platinum group elements within natural magmatic sulfide ore systems. Platinum Met. Rev. 54 (1), 26–36.

Holwell, D.A., Keays, R.R., McDonald, I., Williams, M.R., 2015. Extreme enrichment of Se, Te, PGE and Au in Cu sulfide microdroplets: evidence from LA-ICP-MS analysis of sulfides in the Skaergaard Intrusion, east Grenland. Contrib. Mineral. Petrol. 170, 53. DOI: 10.1007/s00410-015-1203-y.

Kosyakov, V.I., Sinyakova, E.F., 2010. Primary, secondary, and admixture zonation of copper-nickel ores during fractional crystallization of sulfide melts. Dokl. Earth Sci. 432 (2), 829–834.

Kosyakov, V.I., Sinyakova, E.F., 2011. Preparation of eutectics by directional solidification of quaternary melts. Inorg. Mater. 47: 660. DOI: 10.1134/S002016851105013X.

Kosyakov, V.I., Sinyakova, E.F., 2014. Melt crystallization of $CuFe_2S_3$ in the Cu–Fe–S system. J. Therm. Anal. Calorim. 115 (1), 511–516.

Kosyakov, V.I., Sinyakova, E.F., 2015. Peculiarities of behavior of trace elements during fractional crystallization of sulfide magmas. Dokl. Earth Sci. 460 (2), 179–182.

Kosyakov, V.I., Sinyakova, E.F., 2017a. Experimental modeling of pentlandite-bornite ore formation. Russian Geology and Geophysics (Geologiya i Geofizika) 58 (10), 1211–1221 (1528—1541).

Kosyakov, V.I., Sinyakova, E.F., 2017b. Study of crystallization of nonstoichiometric isocubanite $Cu_{1.1}Fe_{2.0}S_{3.0}$ from melt in the system Cu–Fe–S. J. Therm. Anal. Calorim. 129 (2), 623–628.

Lavrent'ev, Yu.G., Karmanov, N.S., Usova, L.V., 2015a. Electron probe microanalysis of minerals: Microanalyzer or scanning electron microscope? Russian Geology and Geophysics (Geologiya i Geofizika) 56 (8), 1154–1161 (1473–1482).

Lavrent'ev, Yu.G., Korolyuk, V.N., Usova, L.V., Nigmatulina, E.N., 2015b. Electron probe microanalysis of rock-forming minerals with a JXA-8100 electron probe microanalyzer. Russian Geology and Geophysics (Geologiya i Geofizika) 56 (10), 1428–1436 (1813–1824).

Likhachev, A.P., 2006. Platinum-Copper-Nickel and Platinum Deposits [in Russian]. Eslan, Moscow.

Makovicky, E., 2002. Ternary and quaternary phase systems with PGE, in: Cabri, L.J. (Ed.), The Geology, Geochemistry, Mineralogy and Mineral Beneficiation of Platinum-Group Elements. Can. Inst. Mining, Metallurgy and Petroleum, Spec. Vol. 54, pp. 131–175.

Massalski, T.B., Okamoto, H., Subramanian, P.R., Kacprzak, L. (Eds.), 1990. Binary Alloy Phase Diagrams (second edition). ASM International, Materials Park, Novelty.

Naldrett, A.J., 2004. Magmatic Sulfide Deposits. Geology, Geochemistry and Exploration. Springer-Verlag, Heidelberg.

Okamoto, H., 2004. Fe–Pt (iron–platinum). J. Phase Equilib. Diffus. 25 (4), 395–399.

Peregoedova, A.V., Fedorova, Zh.N., Sinyakova, E.F., 1995. Physycochemical condition of the pentlandite formation in Cu-bearing sulfide paragenesis (according to experimental data). (Russian Geology and Geophysics) Geologiya i Geofizika 36 (3), 98–105 (91–98).

Ryabchikov, I.D., 1965. Thermodynamic Analysis of the Behavior of Minor Elements during Crystallization of Silicate Melts [in Russian]. Nauka, Moscow.

Sinyakova, E.F., Kosyakov, V.I., 2001. 600 °C section of the Fe–FeS–NiS–Ni phase diagram. Neorganicheskie Materialy 37 (11), 1130–1137.

Sinyakova, E.F., Kosyakov, V.I., 2012. The behavior of noble-metal admixtures during fractional crystallization of As- and Co-containing Cu–Fe–Ni sulfide melts. Russian Geology and Geophysics (Geologiya i Geofizika) 53 (10), 1055–1076 (1374–1400).

Sinyakova, E.F. Kosyakov, V.I., 2014. The polythermal section of the Cu–Fe–Ni–S phase diagram constructed using directional crystallization and thermal analysis. J. Therm. Anal. Calorim. 117 (3), 1085–1089.

Sinyakova, E., Kosyakov, V., Distler, V., Karmanov, N., 2016. Behavior of Pt, Pd, and Au during crystallization of Cu-rich magmatic sulfides. Can. Mineral. 54 (2), 491–509.

Sinyakova, E.F., Kosyakov, V.I., Borisenko, A.S., 2017. Effect of the presence of As, Bi, and Te on the behavior of Pt metals during fractionation crystallization of sulfide magma. Dokl. Earth Sci. 477 (2), 1422–1425.

Sluzhenikin, S., Mokhov, A., 2015. Gold and silver in PGE–Cu–Ni and PGE ores of the Noril'sk deposits, Russia. Miner. Deposita 50 (4), 465–492.

Vymazalova, A., Laufek, F., Kristavchuk, A.V., Drabek, M., 2015. The system Ag–Pd–Te phase relation and mineral assemblages. Miner. Mag. 79 (7), 1813–1832.

Zhmodik, S.M., Nesterenko, G.V., Airiyants, E.V., Belyanin, D.K., Kolpakov, V.V., Podlipsky, M.Yu., Karmanov, N.S., 2016. Alluvial platinum-group minerals as indicators of primary PGE mineralization (placers of southern Siberia). Russian Geology and Geophysics (Geologiya i Geofizika) 57 (10), 1437–1464 (1828–1860).

Editorial responsibility: V.N. Sharapov